Revision 2 Word Count: 11076

Fluid-rock interaction and fluid mixing in the large Furong tin deposit, South China: New insights from tourmaline and apatite chemistry and in situ B−Nd−Sr isotope composition

Shao-Cong Chen[1, 2], Jin-Jie Yu[1*], Min-Feng Bi[1], Bernd Lehmann[3]

1. MNR Key Laboratory of Metallogeny and Mineral Assessment, Institute of Mineral Resources, Chinese Academy of Geological Sciences, Beijing 100037, China
2. School of Earth Resources, China University of Geosciences, Wuhan 430074, China
3. Mineral Resources, Clausthal University of Technology, Adolph–Roemer–Strasse 2A, Clausthal–Zellerfeld 38678, Germany

*Corresponding authors: yjjchina@sina.com (J-J, Yu).

Abstract

The Furong tin deposit (South China) is genetically associated with the multiphase Qitianling batholith that consists of main-phase and minor but more fractionated late-phase granites. Several tourmaline and apatite generations are distinguished. Tourmaline (Tur) variants comprise pre-ore Tur-1 as disseminations and nodules in the late-phase granite, pre- to syn-ore Tur-2 as replacements in nodules and as veins

crosscutting the late-phase granite and nodules, syn-ore Tur-3 in tin greisens, pre- to syn-ore Tur-4 as veins in the altered main-phase granite, and syn-ore Tur-5 from tin skarns in a distinct Ca-rich environment. Apatite (Ap) generations include accessory Ap-G in the main-phase granite, and Ap-I to Ap-III from three stages related to skarn-type mineralization (garnet-diopside stage-I, pargasite-phlogopite-cassiterite stage-II, and sulfide-rich stage-III). Textural and compositional features suggest that all tourmaline variants are hydrothermal in origin with alkali and schorl to foitite composition and minor extensions to calcic and X-site vacant tourmaline groups, whereas all apatite generations belong to fluorapatite with Ap-G crystallizing from the magma and Ap-I to Ap-III being hydrothermal in origin. The narrow range of tourmaline $\delta^{11}B$ values (−14.8 to −10.4 ‰) suggests a single magmatic boron source in the ore-forming fluids. The similar rare earth element patterns and $\varepsilon_{Nd(t)}$ values (−8.2 to −5.9 for Ap-G and −8.0 to −7.3 for Ap-I) between magmatic and hydrothermal apatite indicate that the skarn-forming fluids are dominantly derived from granites. The $^{87}Sr/^{86}Sr$ ratios of Ap-I to Ap-III (0.70733–0.70795) are similar to the carbonate wall rocks, but distinctly different from the more radiogenic granites, indicating Sr exchange with carbonate rocks. Integrating previous H−O isotopic data, the tourmaline and apatite elemental and B−Sr−Nd results suggest that the greisen-type ore formed by interaction of B-, Na-, Li-, Zn-, and Sn-rich magmatic fluids with the late-phase granite in a closed and reduced feldspar-destructive environment, whereas the tin skarns resulted from mixing of

magmatic fluids with meteoric water and interaction with the carbonate wall rocks in an open system where oxygen fugacity changed from reduced to oxidized conditions. During fluid-rock interactions and fluid mixing, considerable Ca, Mg, V, Ni, and Sr from the host rocks were introduced into the ore system. Coupled hydrothermal minerals such as tourmaline and apatite have great potential to fingerprint the nature, source, and evolution of fluids in granite-related ore systems.

Key words: Tourmaline and apatite chemistry, B–Sr–Nd isotopes, fluid tracer; fluid-rock interaction and fluid mixing; tin deposits

Introduction

Constraining the nature, source, and evolution of ore-forming fluids remains challenging, due to the restriction of H–O isotopes to just a few favorable mineral species and difficulty in identifying primary fluid inclusions and their paragenesis (Legros et al. 2018; Andersson et al. 2019). The chemical and isotopic records in hydrothermal minerals thus provide an alternative way to resolve this issue (Jiang et al. 1999; Su et al. 2016; Legros et al. 2018; Codeço et al. 2021). Tourmaline and apatite have been considered as two of the best minerals for this role, due to their broad range in elemental composition and retention of chemical and isotopic signatures (Harlov 2015; Andersson et al. 2019; Dutrow and Henry 2018). Recent advances of analytical techniques, such as laser ablation–inductively coupled plasma–mass spectrometry (LA–ICP–MS),

LA–MC–ICP–MS (MC = multi–collector), and secondary ion mass spectrometry, also permit high-precision in situ analyses of trace elements and B–Sr–Nd isotopes in tourmaline and apatite, which can provide detailed information on the fluid environment during crystal growth (Slack and Trumbull 2011; Zhao et al. 2015). However, an important precondition to use them as aids in deciphering ore genesis is the clear temporal-spatial link between tourmaline/apatite and ore minerals. Tourmaline in granite-related Sn deposits is usually paragenetically early and partly formed prior to tin ores (Trumbull et al. 2020). So far, there are still relatively few studies on syn-ore tourmaline from Sn deposits (Jiang et al. 2004; Duchoslav et al. 2017; Harlaux et al. 2020). Apatite has been widely used to constrain the petrogenesis of igneous rocks (Sha and Chappell 1999; Chu et al. 2009), discriminate mineralized from barren intrusions (Belousova et al. 2002; Cao et al. 2011), and decipher the ore-forming processes of iron-oxide apatite, iron-oxide copper gold, porphyry and skarn W–Cu deposits (Zeng et al. 2016; Adlakha et al. 2018; Cao et al. 2021). However, apatite chemistry as a potential indicator for granite-related Sn mineralization has rarely been explored.

The large Furong Sn deposit (530,000 t Sn at 0.8 % Sn) in the Nanling Range, South China, is associated with the Mid–Late Jurassic Qitianling granite batholith of A-type and ilmenite-series affinity (Fig. 1; Mao et al. 2004; Yuan et al. 2011; Zhao et al. 2012; Chen et al. 2021a). Tin greisens and skarns are dominant in this deposit, with cassiterite U–Pb ages of ~158 Ma (Yuan et al. 2011; Wang et al. 2014), consistent with the zircon U–Pb

ages of 163–153 Ma for the Qitianling granites (Zhu et al. 2009; Chen et al. 2021a). At Furong, tourmaline widely occurs as disseminated grains, nodules, vein fill, and replacements in granites and tin ores, and apatite is observed in granites, skarns, and tin ores, providing the opportunity to unravel the nature, source, and evolution of the ore-forming fluids. Yang et al. (2015) proposed that the disseminated, nodular, to veinlet/vein tourmaline in the Qitianling batholith, about 10 km to the north of the Furong deposit, represented an idealized sequence from parental granite through magmatic-hydrothermal transition and finally to hydrothermal stages. However, tourmaline stability in granitic systems depends on the Al saturation of the melt, and tourmaline is strongly unstable in granitic systems with $Al_2O_3/(CaO+Na_2O+K_2O)$ (A/CNK) < 1.2 at 700–750°C, regardless of the B content of the melt (Wolf and London 1997). The Qitianling granites have A/CNK values lower than 1.1 and zircon saturation temperatures of 747–860°C (Chen et al. 2021a). Besides, the Qitianling granites have whole-rock B contents of 14−37 ppm (Zhao et al. 2011), much lower than the minimum B contents of 500−3000 ppm to achieve tourmaline saturation even for peraluminous granitic melts (Pesquera et al. 2013). Thus, it is unlikely for the Qitianling magma to reach tourmaline saturation, and the tourmaline origin should be reconsidered. Also, the relationship between hydrothermal tourmaline in the samples by Yang et al. (2015) and tin mineralization is unclear.

This work presents paragenetic information, micro-textures, in situ elemental, and

B–Sr–Nd isotopic compositions of tourmaline and apatite at the Furong deposit. These data allow us to constrain the origin of the Furong deposit, and highlight the suitability of coupled tourmaline and apatite as tracers of the nature, source, and evolution of ore-forming fluids in granite-related ore systems.

Geologic setting

The Nanling Range is located in central South China, which is developed by amalgamation of the Yangtze and Cathaysia Blocks at ~900 Ma along the Jiangshan–Shaoxing fault zone in the northeast and Chenzhou–Linwu fault zone in the southwest (Fig. 1a; Li et al. 2009; Wang et al. 2013). The regional NNE-trending Chenzhou–Linwu fault runs across the Nanling Range (Fig. 1b). The basement of the Nanling Range comprises Neoproterozoic to Silurian low-grade metamorphic clastic sedimentary rocks, covered by Devonian to Cretaceous clastic, carbonate, and volcanic rocks (Fig. 1b; Yuan et al. 2019). Besides minor Devonian–Triassic granites, the Mid–Late Jurassic (165–150 Ma) granites cover the largest map area (Fig. 1b; Gilder et al. 1996; Li et al. 2018) and are closely associated with Sn–W mineralization, such as the world-class Shizhuyuan, Xianghualing, Xitian, Xihuashan, and Furong deposits, forming one of the world's most important Sn–W provinces (Fig. 1b; Mao et al. 2013; Yuan et al. 2019).

The Furong Sn deposit occurs at the southern margin of the Qitianling batholith

(Figs. 1b and 1c). The exposed strata mainly comprise Carboniferous to Permian clastic and carbonate rocks with minor Triassic carbonate rocks, which are folded with NNE-trending fold axes (Fig. 1c). Faults in the Furong deposit are mainly NNE- and NE-trending (Fig. 1c). The Qitianling batholith with an exposed area of ~520 km^2 (Figs. 1b and 1c) consists of porphyritic, main-phase, hornblende-biotite and biotite monzogranite (main-phase granite) and minor fine-grained late-phase biotite-siderophyllite alkali-feldspar granite (late-phase granite). The two granite phases were coeval with U–Pb ages of 163–153 Ma (Zhu et al. 2009; Chen et al. 2021a), and formed by incremental assembly of multiple magma pulses (Chen et al. 2021a). Compared to the metaluminous main-phase granite with A/CNK values of 0.8–1.0, the late-phase granite has a more evolved and metaluminous to weakly-peraluminous composition with A/CNK values of 1.0–1.1 (Zhao et al. 2012; Chen et al. 2021a).

Tin orebodies at Furong are mainly distributed in the Bailashui-Anyuan (BA; largest resource with 430,000 t Sn at 0.8 % Sn), Heishanli-Maziping (HM), and Shanmenkou-Goutongling zones, from northwest to southeast (Fig. 1c; Mao et al. 2004). Tin mineralization is dominated in greisen- and skarn-types, although some other types are also recognized. Tin mineralization is directly related to the more fractionated late-phase granite, as shown by the intimate spatiotemporal association (Yuan et al. 2011; Chen et al. 2021a). Greisen-type mineralization occurs within the late-phase granite at the HM zone (Fig. 1c). The paragenetic sequence can be subdivided into three main stages

(Appendix 1a (App. 1a)): pre-ore (quartz + albite + K-feldspar + tourmaline), syn-ore (quartz + muscovite + tourmaline + fluorite + cassiterite ± sulfides), and post-ore (calcite + fluorite) stages. At the BA zone, the skarn-type No. 19 orebody is mainly overprinted on an irregular Permian limestone 'raft' inside the main-phase granite, and bounded by two NNE-trending faults (Fig. 2). The mineralization formed in four stages (App. 1b): prograde stage-I (garnet + diopside), retrograde stage-II (vesuvianite + pargasite + phlogopite + fluorite + sellaite + cassiterite + magnetite, the main ore-forming stage), sulfide-rich stage-III (quartz + pyrite + arsenopyrite + chalcopyrite + sphalerite + cassiterite; less important tin mineralization), and late stage-IV (fluorite + calcite).

Tourmaline occurrence and paragenesis

Five types of tourmaline (Tur) were identified at Furong, including Tur-1, Tur-2, and Tur-3 at the HM zone, and Tur-4 and Tur-5 at the BA zone. Their characteristics and paragenesis are summarized as below.

Tur-1 to Tur-3: Pre-ore Tur-1 occurs as disseminations and nodules in the late-phase granite. The disseminated Tur-1 occurs interstitial to quartz, K-feldspar, and albite (Fig. 3a). It is fine-grained and subhedral with tan to blue-green pleochroism (Fig. 3a), and homogeneous in backscattered electron (BSE) images (Fig. 3b). Spherical to elliptic quartz-Tur-1 nodules with varying diameters (0.5–10 cm) are distributed within the late-phase granite (Fig. 3c). The nodules consist of > 50 vol% quartz, and > 45 vol%

tourmaline with minor albite, muscovite, and fluorite (Figs. 3d–3g). They are rimmed by a 0.5–2 cm wide leucocratic halo (Fig. 3c), which contains more K-feldspar, less albite, and is devoid of tourmaline and mafic minerals like biotite and siderophyllite, compared with the late-phase host granite. The nodular Tur-1 is brown in color and includes euhedral quartz and albite grains (Fig. 3d), with a homogeneous BSE image (Fig. 3f). Tur-2 replacements and veins are observed at the pre- to syn-ore stage. Within the nodules, the brown Tur-1 is replaced by blue Tur-2, minor fluorite and muscovite (Fig. 3e), when muscovite replaces albite (Fig. 3g). The nodular Tur-2 is characterized by pitted surfaces with visible voids and tiny fluorite inclusions (Figs. 3e and 3f). Locally, it is included by or intergrown with arsenopyrite (Fig. 3h), indicating its formation at the pre- to syn-ore stage. Quartz-Tur-2 veins with mafic mineral-absent, leucocratic halos crosscut the late-phase granite and locally the Tur-1 nodules (Fig. 3i), indicating that the vein-type Tur-2 postdates Tur-1. It also coexists with minor muscovite (Fig. 3j). It shows pleochroism from orange to yellow-green and blue (Fig. 3j), and has weak patchy zoning in BSE images (Fig. 3k). Syn-ore Tur-3 occurs in greisen-type ores. Anhedral to subhedral and fine-grained Tur 3 co-exists with abundant cassiterite and muscovite (Figs. 3l and 3m). It is bluish to light brown in color (Fig. 3l), and shows weak oscillatory zoning in BSE images (Fig. 3m). Locally, Tur-3 co-exists with arsenopyrite (Fig. 3n) and chalcopyrite (Fig. 3o). It shows tan to blue-green pleochroism (Fig. 3n) with a homogeneous BSE image (Fig. 3o).

This is the peer-reviewed, final accepted version for American Mineralogist, published by the Mineralogical Society of America.
The published version is subject to change. Cite as Authors (Year) Title. American Mineralogist, in press.
DOI: https://doi.org/10.2138/am-2022-8310. http://www.minsocam.org/

Tur-4 to Tur-5: A 30–60 cm wide quartz-Tur-4 vein crosscuts the main-phase granite (Fig. 4a). Along the vein occur leucocratic halos (Fig. 4a), in which plagioclase is intensively replaced by sericite. Tur-4 consists mainly of radiating, coarse-grained, euhedral prismatic crystals (Fig. 4b), comprising dark bluish cores and dark tan rims (Fig. 4b). It shows oscillatory zoning in BSE images (Fig. 4c). Tur-4 is locally intergrown with or replaced by muscovite (Fig. 4d) and sphalerite (Fig. 4e), implying that it formed at the pre- to syn-ore stage. Tur-5 co-exists with pargasite, fluorite, and cassiterite, replacing vesuvianite in the stage-II skarn-type ore (Fig. 4f). It is bluish to blue in color (Fig. 4f) with patchy zoning in BSE images (Fig. 4g).

Apatite occurrence and paragenesis

Four apatite (Ap) generations were distinguished at the BA zone, including Ap-G in the unaltered main-phase granite away from the quartz-Tur-4 veins, and Ap-I, Ap-II, and Ap-III from stages-I to III related to the skarn-type mineralization. Apatite is not observed at the HM zone. The apatite characteristics and paragenesis are summarized as below.

Ap-G: As an ubiquitous accessory mineral in the main-phase granite, Ap-G has subhedral to euhedral, tabular, and locally hexagonal shape, with crystals up to 400 μm long and 100 μm wide (Fig. 5a). Ap-G is generally included by biotite (Fig. 5a). Regardless of the very narrow rims that are unanalyzable by LA(–MC)–ICP–MS, Ap-G mainly displays yellow-green to light green luminescence in cathodoluminescence (CL)

images (Fig. 5b), and is relatively homogeneous and bright in BSE images (Fig. 5c).

Ap-I to Ap-III: Ap-I is observed in stage-I garnet skarn (Fig. 5d). It occurs as subhedral to anhedral fine grains (up to 100 μm in diameter), and is mainly blue with very narrow green rims in CL images (Fig. 5e), and homogeneous in BSE images (Fig. 5f). Apatite also occurs interstitial to diopside grains in the diopside-pargasite skarn, and it is relatively large with diameter of up to 600 μm (Fig. 5g). It displays zoning textures with blue cores and green rims in CL images (Fig. 5h). In BSE images, the cores are brighter than the rims (Fig. 5i). The co-existing diopside is replaced by pargasite (Figs. 5g and 5i). Thus, the blue cores are considered to be Ap-I, whereas the green rims are categorized as Ap-II. In addition, Ap-II disseminations and veinlets also occur in stage-II skarn-type tin ores, and show an intimate association with pargasite, fluorite, and cassiterite (Fig. 5j). In CL images, Ap-II dominantly shows green luminescence, and locally has very small blue cores (Fig. 5k), which is very weak to indiscernible in high-contrast BSE images (Fig. 5l). Subhedral to anhedral fine-grained Ap-III co-exists with sphalerite at the sulfide-rich stage-III (Fig. 5m). It displays green luminescence, or color zonation with light bluish grey cores and green rims in CL images (Fig. 5n), but is homogeneous in BSE images (Fig. 5o).

Samples and analytical methods

Ten tourmaline-bearing samples (Fig. 1c) and eight apatite-bearing samples (Fig. 2)

This is the peer-reviewed, final accepted version for American Mineralogist, published by the Mineralogical Society of America.
The published version is subject to change. Cite as Authors (Year) Title. American Mineralogist, in press.
DOI: https://doi.org/10.2138/am-2022-8310. http://www.minsocam.org/

were collected from the Furong deposit. After a detailed examination of tourmaline and apatite micro-textures under BSE and optical CL images, in situ major- and trace-elemental compositions of both minerals were measured by electron probe microanalysis (EPMA) and LA–ICP–MS, respectively. In situ tourmaline B and apatite Sr–Nd isotope spot analyses were then determined using LA–MC–ICP–MS. The analytical methods are described in App. 2.

Results

Major- and trace-elemental composition of tourmaline

Major- and trace-elemental compositions of the Furong tourmaline are given in App. 3, and the average elemental compositions of selected elements are summarized in Table 1. The analyzed tourmaline mostly plots in the alkali group and has schorlitic composition, with a minor subset belonging to the calcic and X-site vacant groups and foitite (Figs. 6a–6c; Henry and Guidotti 1985; Henry et al. 2011). At the HM zone, Tur-1 and Tur-2 have similar compositions, but Tur-2 from the nodules has slightly lower Mg and F than the corresponding Tur-1 from individual crystals (Figs. 7a and 7b), and minor Tur-2 shows Ca, Fe/(Fe+Mg), Mg, and F close to Tur-3 (Table 1; Figs. 6a−6f). Compared to Tur-1, Tur-3 has higher Ca, $X_{\square}$ (vacancy in X-site), Mg, lower Fe/(Fe+Mg), Fe, F, and similar Al contents (Table 1; Figs. 6a−6f). Relative to tourmaline variants at the HM zone,

This is the peer-reviewed, final accepted version for American Mineralogist, published by the Mineralogical Society of America.
The published version is subject to change. Cite as Authors (Year) Title. American Mineralogist, in press.
DOI: https://doi.org/10.2138/am-2022-8310. http://www.minsocam.org/

241 Tur-4 at the BA zone exhibits high Ca, $X_{\square}$, Mg, Al, and low Fe/(Fe+Mg), Fe, F contents,
242 while Tur-5 is characterized by the highest Ca, high but variable Fe, Mg, and low
243 Fe/(Fe+Mg), Al, $X_{\square}$, F contents (Table 1; Figs. 6a−6f).

244 Tourmaline at Furong has relatively high concentrations (several to thousands of
245 ppm) of Li, Be, Sc, V, Cr, Co, Ni, Zn, Ga, Sr, and Sn, with concentrations of other trace
246 and rare earth elements (REE) analyzed generally low or below the detection limit (App.
247 3). At the HM zone, Tur-1 and Tur-2 have similar abundances in most trace elements, but
248 the latter shows slightly lower Li and higher Sn, close to Tur-3 (Table 1; Figs. 6g–6l).
249 Compared to the nodular Tur-1, the corresponding Tur-2 from individual crystals has
250 lower Li, Sc, Zn, and higher Sn (Figs. 7c–7f). Relative to Tur-1, Tur-3 has lower Li, Zn,
251 higher V, Sr, Sn, and similar Ni contents (Table 1; Figs. 6g–6l). At the BA zone, Tur-4
252 and Tur-5 have high V, Ni, Sr, and Sn concentrations, with the former showing the lowest
253 Li and Zn (Table 1; Figs. 6g–6l).

254 **Boron isotope composition of tourmaline**

255 The B isotope compositions of the Furong tourmaline are shown in Fig. 8a, and the
256 full dataset is reported in App. 4. The measured $\delta^{11}B$ values of all tourmaline types vary
257 narrowly from −14.8 to −10.4 ‰ (N=106) (Fig. 8a). Tur-2 in the nodules has higher $\delta^{11}B$
258 values than the corresponding Tur-1 from individual crystals (Fig. 8b).

This is the peer-reviewed, final accepted version for American Mineralogist, published by the Mineralogical Society of America.
The published version is subject to change. Cite as Authors (Year) Title. American Mineralogist, in press.
DOI: https://doi.org/10.2138/am-2022-8310. http://www.minsocam.org/

259 **Major- and trace-elemental composition of apatite**

260 Major- and trace-elemental compositions of the Furong apatite are given in App. 5,
261 and the average compositions of selected elements are summarized in Table 2. Four
262 apatite types exhibit no systematic difference in CaO and P_2O_5 contents (Table 2), and all
263 of them belong to fluorapatite with high F concentrations of 2.4−4.3 wt% and low SiO_2,
264 SO_3, TiO_2, Al_2O_3, BaO, Na_2O, K_2O, and Cl concentrations (Table 2).

265 Trace elements like Na, Fe, Mn, V, Ga, Sr, Y, REE, Pb, Th and U in the Furong
266 apatite were always detected (Table 2), whereas other elements analyzed were mostly
267 below the detection limit. Ap-G has high Fe, Mn, Ga, Na, REE, Y, and low V, Sr, Th, U
268 contents, Sr/Y ratios (Fig. 9). It shows light REE (LREE)-enriched chondrite-normalized
269 REE patterns, with La_N/Yb_N ratios of 5.4−13.1 and extremely negative Eu anomaly (δEu
270 < 0.1; Table 2; Fig. 10a). In contrast, Ap-I to Ap-III from skarns generally have high V, Sr,
271 Th, U, and Sr/Y, and low Na, Fe, Mn, Ga, REE, and Y concentrations (Fig. 9). Their REE
272 patterns are also LREE-enriched but with higher La_N/Yb_N ratios of 13.2−87.0 and δEu
273 mostly of 0.3−0.7 (Table 2; Figs. 10b and 10c). Besides, Ap-II has slightly lower REE
274 and Y than Ap-I (Table 2; Figs. 9c and 9e).

275 **Sr–Nd isotope composition of apatite**

276 A total of 51 Sr isotopic spot analyses were obtained from Ap-I to Ap-III, whereas Sr
277 contents of Ap-G are too low for in-situ Sr isotopic analysis by the LA−MC−ICP−MS

technique. Thirty-six spots of Nd isotopic analyses were conducted on Ap-G and Ap-I, but the Nd isotopic composition of the other Nd-poor apatite types is unmeasurable. The apatite Sr−Nd isotopic results are listed in App. 6.

Ap-I to Ap-III have extremely low Rb/Sr ratios (<0.01; App. 6), so that their present-day $^{87}Sr/^{86}Sr$ ratios are not significantly affected by ^{87}Rb decay and provide a record of the initial Sr isotopic signatures. Ap-I to Ap-III have mutually indistinguishable $^{87}Sr/^{86}Sr$ ratios ranging from 0.70733 to 0.70795 (Fig. 11a). The $\varepsilon_{Nd(t)}$ values of Ap-G and Ap-I were calculated for 160 Ma (zircon U−Pb age for the main-phase granite; Zhu et al. 2009) and 158 Ma (cassiterite U−Pb age for tin mineralization; Yuan et al. 2011), respectively. Ap-G and Ap-I have overlapping $\varepsilon_{Nd(t)}$ values of −8.2 to −5.9 and two-stage model ages (T_{DM2}) of 1428−1615 Ma (Fig. 11b).

Discussion

Tourmaline and apatite origin

High-temperature hydrothermal overprint (i.e., subsolidus alteration) during the magmatic-hydrothermal transition is seen in the Qitianling late-phase granite, as shown by the occurrence of turbid albite and high-U, structure-damaged zircons (Haapala 1997; Zhang et al. 2017), and the extremely low whole-rock Nb/Ta ratios (down to 2.9) and REE tetrad effects (Chen et al. 2021a). Considering the instability of tourmaline in the

297 metaluminous to weakly peraluminous late-phase granite, we infer that the disseminated
298 Tur-1 at the HM zone (Fig. 3a) is formed during the subsolidus alteration process, similar
299 to siderophyllite from highly-evolved granites related to rare-metal mineralization
300 (Mohamed et al. 1999). The leucocratic halos surrounding Tur-1 nodules (Fig. 3c)
301 suggest crystallization of the nodular Tur-1 favored by decomposition of biotite and
302 siderophyllite, possibly at subsolidus conditions (Wolf and London 1997; Harlaux et al.
303 2020). The similar compositions between the disseminated and nodular Tur-1 subtypes
304 also suggest the same hydrothermal origin. Tur-2 occurs as replacements in tourmaline
305 nodules (Fig. 3e) and as veins crosscutting the late-phase granite and nodules (Fig. 3i). It
306 co-exists with muscovite (Figs. 3g and 3j) and fluorite (Figs. 3e and 3f). Tur-2
307 replacements particularly show systematic differences in elemental and B isotopic
308 compositions compared to the nodular Tur-1 (Figs. 7 and 8b), suggesting a hydrothermal
309 origin for Tur-2. Tur-3 in tin greisens was formed during interaction of hydrothermal
310 fluids with the late-phase granite, which was accompanied by precipitation of muscovite,
311 cassiterite, and/or sulfides (Figs. 3l–3o). At the BA zone, Tur-4 occurs as veins
312 crosscutting the main-phase granite (Fig. 4a), and Tur-5 replaces vesuvianite in the
313 stage-II skarn-type ore (Fig. 4f). Both of them show contrasting compositions compared
314 to Tur-1 to Tur-3 at the HM zone (Fig. 6), indicating a hydrothermal origin for Tur-4 and
315 Tur-5 in a different host-rock environment. The distinct and complex chemical
316 environment for the skarns explains the heterogeneous composition of Tur-5. Hence, all

317 five tourmaline variants are of hydrothermal origin.

318 In the main-phase granite, accessory Ap-G has high F, Fe, Mn, Ga, REE, and Y, and
319 low V and Sr contents (Table 2; Figs. 9a−9e), features typical of magmatic apatite from
320 granitoids (Sha and Chappell 1999; Chu et al. 2009). In the Mn−Sr, Y−Sr, and
321 LREE−Sr/Y diagrams (Figs. 9b, 9c and 9f; Belousova et al. 2002; O'Sullivan et al. 2020),
322 Ap-G plots mostly in the granite, granite pegmatite, and alkali-rich igneous rocks fields.
323 Based on the parent rock REE concentrations (Zhao et al. 2012; Chen et al. 2021a) and
324 $D_{REE}^{ap/melt}$ (Fujimaki 1986), the calculated REE abundances for ideal apatite equilibrated
325 with the main-phase granite show identical patterns to the measured results (Fig. 10a).
326 Besides, Ap-G shares similar Nd isotopic characteristics to the host granite (Fig. 11b;
327 Zhao et al. 2012). Thus, Ap-G is magmatic in origin. In contrast, the skarn-hosted Ap-I to
328 Ap-III (Figs. 5d−5o) have distinctly different elemental compositions from Ap-G (Fig. 9).
329 They plot out of the granite-related fields in the Mn−Sr and Y−Sr diagrams (Figs. 9b and
330 9c), and extend to the hydrothermal apatite field in the LREE−Sr/Y diagram (Fig. 9f).
331 They also show right-inclined REE patterns (Figs. 10b and 10c), comparable to
332 hydrothermal apatite from skarns elsewhere (Adlakha et al. 2018). These features
333 demonstrate they are of hydrothermal origin. In summary, Ap-G at Furong crystallized
334 directly from the magma, whereas skarn-hosted Ap-I to Ap-III are hydrothermal in origin.
335

Source of the magma and ore-forming fluids

The magmatic Ap-G has $\varepsilon_{Nd(t)}$ and T_{DM2} values similar to the whole-rock data for the Qitianling granites (Fig. 11b; Zhao et al. 2012; Chen et al. 2021a), supporting the previous conclusion that the magma derived from partial melting of an old crustal source with minor involvement from a mafic magma (Zhao et al. 2012; Chen et al. 2021a).

All tourmaline variants at Furong have consistent $\delta^{11}B$ values (−14.8 to −10.4 ‰; Fig. 9a), overlapping with the whole-rock data (−14.0 to −10.9 ‰, N=5) for the Qitianling granites (Fig. 12a; Zhao et al. 2011), and those of tourmalines from granite-related systems worldwide (Fig. 12a; Marschall and Jiang 2011). This suggests a single magmatic boron source in the ore-forming fluids. The temperature-dependent tourmaline-fluid B isotope fractionation (Meyer et al. 2008) is used to calculate the $\delta^{11}B_{fluid}$ values. The quartz-tourmaline oxygen isotope thermometer has yielded crystallization temperatures of ~650°C for disseminated and nodular tourmaline at the magmatic-hydrothermal transition, and ~550°C for tourmaline as post-magmatic replacements and veins in tin-bearing granites elsewhere (Harlaux et al. 2021). These temperatures are adopted for Tur-1 and Tur-2/Tur-4 in this study, respectively (App.4). Fluid inclusions in quartz have homogenization temperatures of ~350°C for the Tur-3-bearing tin greisens, and ~400°C for the Tur-5-bearing tin skarns at Furong (Shuang et al. 2009). These microthermometric data are used without pressure correction because fluid boiling was observed (Shuang et al. 2009).

This is the peer-reviewed, final accepted version for American Mineralogist, published by the Mineralogical Society of America.
The published version is subject to change. Cite as Authors (Year) Title. American Mineralogist, in press.
DOI: https://doi.org/10.2138/am-2022-8310. http://www.minsocam.org/

At the HM zone, the calculated $\delta^{11}B_{fluid}$ values increase from −13.7 to −11.6 ‰ (avg. −12.7 ‰) for the pre-ore fluid, through −13.2 to −8.8 ‰ (avg. −11.6 ‰) for the pre- to syn-ore fluid, to −11.3 to −9.6 ‰ (avg. −10.4 ‰) for the syn-ore fluid (App. 4; Fig. 12b). This small increase in $\delta^{11}B_{fluid}$ values is likely influenced by Rayleigh fractionation in a closed magmatic-hydrothermal system. The similarity in H−O isotopic composition between quartz from tin greisens (δD_{fluid} = −89 to −62 ‰ and $\delta^{18}O_{fluid}$ = 5.5 to 7.6 ‰; Shuang et al. 2009) and typical magmatic fluids (Sheppard 1986) also precludes the ingress of external fluids. Because of the progressive ^{11}B enrichment in the residual fluid during tourmaline precipitation (Jiang et al. 1999; Marschall et al. 2009), the lowest $\delta^{11}B_{fluid}$ value (−13.7 ‰) of the pre-ore fluid is assumed to be the ^{11}B value of the initial magmatic fluid. Model calculations based on Rayleigh fractionation show that the consumption of ~98 to ~73 % at 650−350 °C of the initial boron budgets would increase the $\delta^{11}B$ values of the residual fluid to achieve the largest $\delta^{11}B_{fluid}$ value (−9.6 ‰) of the syn-ore fluid (Fig. 12b).

At the BA zone, the $\delta^{11}B_{fluid}$ values calculated from Tur-4 and Tur-5 range from −12.7 to −9.8 ‰ (avg −11.0 ‰), similar to those at the HM zone (Fig. 12b), indicating the same magmatic origin for the ore-forming fluids with respect to boron. The skarn-hosted Ap-I to Ap-III show REE patterns similar to the magmatic Ap-G, but distinct from the carbonate wall rocks (Fig. 10), suggesting an intimate association between the magma and ore-forming fluids, as supported by the consistence in Nd isotopic

compositions of Ap-I with Ap-G and the Qitianling granites (Fig. 11b). However, Ap-I to Ap-III have $^{87}Sr/^{86}Sr$ ratios (0.70733–0.70795) lower than the Qitianling granites (0.70913–0.71315; Zhao et al. 2012), but similar to Permian carbonate rocks (0.70698–0.70753; Yan and Wu 2004) (Fig. 11a), indicating the significant Sr contribution of the carbonate wall rocks by fluid-rock interaction, and/or the addition of meteoric water that equilibrated with limestone. This is consistent with the $^{87}Sr/^{86}Sr$ ratios of 0.7083–0.7091 (N=11) and $\varepsilon_{Nd(t)}$ of −9.4 to −0.7 (N=10) of separated fluorite from the same orebody (Yuan et al. 2008), although these data vary dramatically. The H–O isotopic compositions for quartz from the stage-III sulfide-rich ores (δD_{fluid} = –67 to –62 ‰ and $\delta^{18}O_{fluid}$ = –5.1 to –1.3 ‰; Shuang et al. 2009) lie between those for magmatic and meteoric waters (Sheppard 1986), implying the involvement of meteoric water at stage-III. Thus, the extremely B-poor carbonate wall rocks and meteoric water (<4 ppm; Pennisi et al. 2000; Xu et al. 2021) have little influenced the magmatic B isotopic system.

In summary, tin greisens at Furong formed in a closed magmatic-hydrothermal system, whereas tin skarns resulted from fluid-rock interaction and mixing between magmatic fluid and wall rock-derived meteoric water. The tourmaline and apatite data are indicative of B, Nd, and Sr contributions from distinct reservoirs.

Nature of the ore-forming fluids

Tourmaline is a robust indicator of its host rocks and fluid environment (van Hinsberg 2011; Hong et al. 2017; Dutrow and Henry 2018). Mineral–fluid trace element partition coefficients allow for the estimating of fluid compositions from the mineral composition (van Hinsberg et al. 2017; Dutrow and Henry 2018). Unfortunately, tourmaline–fluid element partition coefficients ($D^{tur/fluid}$) have not been determined experimentally. As an alternative, they can be calculated by combining experimental tourmaline-melt (van Hinsberg 2011) and fluid-melt (Zajacz et al. 2008; Iveson et al. 2019) D values, following the approach of Keppler (1996) (App. 2). The estimated $D^{tur/fluid}$ values are 0.2, 0.3, 0.1, and 1.9 for Na, Li, Zn, and Sr, respectively (App. 2). As a result, the calculated Na, Li, Zn, and Sr concentrations in the fluids fall in the range of 2.8−7.1 wt%, 24−1224 ppm, 782−3619 ppm, and 0−229 ppm, respectively (App. 3; Table 1). They are comparable to the analytical results by LA−ICP−MS on single fluid inclusions and estimations by mica compositions from granite-related tin deposits elsewhere (Audétat et al. 2000a, 2000b; Müller et al. 2001; Codeço et al. 2021). Tin contents in the fluids cannot be obtained due to lack of a $D_{Sn}^{tur/melt}$ value. However, all tourmaline variants at Furong have much higher Sn contents (avg 107−435 ppm; Table 2) than their host rocks (avg <25 ppm for bulk rock; Zhao et al. 2012; Wang et al. 2014; Chen et al. 2021a), probably indicating a Sn-rich fluid that exsolved from granitic melts (Heinrich 1990; Lehmann 1990, 2021). Thus, the ore-forming fluids at Furong are rich in

415 B, Na, Li, Zn, and Sn, but relatively poor in Sr.

416 At the HM zone, the depletion of Li in Tur-2 and Tur-3 relative to Tur-1 (Table 1;
417 Fig. 6g) are accompanied by the presence of muscovite (Figs. 3g, 3j, 3l, and 3m), which
418 preferentially incorporates Li from the fluids due to the large partition coefficient
419 ($D_{Li}^{muscovite/tur}$ of ~5.3; van Hinsberg et al. 2017). Similarly, the decreasing Fe, F, and Zn
420 from Tur-1 and Tur-2 to Tur-3 (Table 1; Figs. 6c, 6f and 6k) can be explained by their
421 preferential incorporation into co-existing Fe-rich cassiterite (our unpublished data),
422 fluorite and sulfides, respectively (App.1; Figs. 3l–3o), although the X-site charge may
423 also have an influence on F incorporation into tourmaline (Henry and Dutrow 2011). In
424 contrast, the Mg, Ca, V, and Sr rise from Tur-1 and Tur-2 to Tur-3 (Table 1; Figs. 6a, 6c,
425 6h and 6j) imply the depletion of these components in the pre-ore fluid and addition of
426 these components from the late-phase host granite by decomposition of mica and feldspar
427 during greisenization. Tin is more enriched in Tur-2 and Tur-3 than in Tur-1 (Table 1; Fig.
428 6l). Some Sn would be released during the alteration of granites, but could be transported
429 only over relatively short distances before precipitation as cassiterite (Schmidt et al.
430 2020). In a series of experiments, Zhao et al. (2021) determined fluid/melt partition
431 coefficients (1.9–35) for Sn and found that a fluid could efficiently extract Sn during fluid
432 exsolution especially during the late-stage of magmatic evolution. Given that rare or no
433 cassiterite coexists with the Sn-rich Tur-2, we ascribe the increasing Sn content with fluid
434 evolution to late Sn-rich magmatic fluid pulses.

435 At the BA zone, Ca enrichment in Tur-4 and Tur-5 relative to Tur-1 to Tur-3 (Fig.
436 6a), and the presence of abundant apatite and other Ca-rich skarn minerals (Figs. 5d–5o),
437 indicate a Ca-rich environment. Considering the Sn-poor main-phase granite (avg 16 ppm;
438 Zhao et al. 2012) and carbonate wall rocks (mostly <1 ppm; Wang et al. 2014), the strong
439 Sn enrichment in Tur-4 and Tur-5 (Fig. 6l) may reflect a strongly Sn-rich fluid, consistent
440 with the large tin reserve in this zone. Depletion of F, Li, and Zn in Tur-4 (Figs. 6f, 6g
441 and 6k) can be ascribed to the occurrences of fluorite, muscovite (Fig. 4d), and sphalerite
442 (Fig. 4e), respectively. Tur-4 is characterized by high Ca, Mg, V, Ni, and Sr contents
443 (Table 1; Figs. 6a, 6c, and 6h–i), consistent with the composition of its main-phase host
444 granite (Zhao et al. 2012). This probably demonstrates a derivation of these components
445 from the host rocks. The highest Ca and high Mg, V, Ni, and Sr concentrations in
446 skarn-hosted Tur-5 (Figs. 6a, 6c, and 6h–j) coincide with the composition of carbonate
447 wall rocks (Wang et al. 2014). This indicates the significant contribution of carbonate
448 rocks in these components to the skarn-forming fluids, as shown by the V and Sr
449 enrichment (Figs. 9a–c) and $^{87}Sr/^{86}Sr$ ratios (Fig. 11a) of the skarn-hosted Ap-I to Ap-III.
450 REE and Y are generally leached out of apatite by Cl-rich fluids to form REE mineral
451 inclusions like monazite (Harlov 2015; Andersson et al. 2019), but Na and Ca enrichment
452 in the fluids would suppress the growth of these minerals (Harlov 2015; Zeng et al. 2016).
453 The absence of coexisting REE minerals with Ap-II that replaces Ap-I is consistent with
454 the Na- and Ca-rich fluids at the BA zone.

455 In summary, the ore-forming fluids at Furong are rich in B, Na, Li, Zn, and Sn.
456 During fluid evolution, considerable Ca, Mg, V, Ni, and Sr from the host rocks were
457 added into the ore-forming system by fluid-rock exchange and/or fluid mixing.
458

459 **Oxygen fugacity and ore precipitation**

460 The abundances of redox-sensitive elements in apatite and elemental substitutions in
461 tourmaline have been widely used as oxygen fugacity proxies (Sha and Chappell 1999;
462 Henry and Dutrow 2012; Miles et al. 2014; Dutrow and Henry 2018). Under reduced
463 conditions, apatite is generally enriched in Ga, Mn, and depleted in V contents (Sha and
464 Chappell 1999; Miles et al. 2014). Such features observed in Ap-G (Figs. 9a, 9b and 9d)
465 imply a relatively reduced condition for the Qitianling granites, consistent with their
466 general ilmenite-series affinity and previous estimations from biotite composition and
467 phase equilibrium experiments (~NNO buffer; Huang et al. 2019; Chen et al. 2021a).
468 Although Tur-5 displays scatter in Fig. 6c, compositional variabilities in all the
469 tourmaline variants at Furong generally demonstrate combined substitutions of
470 $(AlO)[R^{2+}(OH)]_{-1}$, $(AlO)(R^{2+}F)_{-1}$, $(X_{\square}Al)(NaR^{2+})_{-1}$, and $({}^{Y}Al{}^{T}Al)(R^{2+}Si)_{-1}$, where R
471 represents Fe, Mg, and/or Mn, and ^{Y}Al and ^{T}Al are Al at the Y and T sites, respectively
472 (Figs. 6c–6e). Tur-1 and Tur-2 exhibit a dominant substitution of $AlFe^{3+}_{-1}$ (Fig. 6c), which
473 can be ascribed to the extremely low Mg abundances. Importantly, Tur-3 from the tin

474 greisen and Tur-4 from the quartz-Tur-4 vein show both substitutions of $MgFe^{2+}_{-1}$ and
475 $AlFe^{3+}_{-1}$ (Figs. 6c–6e), whereas the skarn-hosted Tur-5 is dominated by $AlFe^{3+}_{-1}$ (Fig. 6e).
476 This indicates a relatively low oxygen fugacity for the greisen-forming fluid at the HM
477 zone, and a transition to higher oxygen fugacity for the skarn-forming fluids at the BA
478 zone (Henry and Dutrow 2012; Dutrow and Henry 2018; Qiu et al. 2021). A relatively
479 reduced condition of the greisen-forming fluid is consistent with the causative Qitianling
480 magma. The skarn-hosted Ap-I to Ap-III has Mn contents (avg 111−149 ppm; Table 2)
481 much lower than apatite from reduced skarns at the Cantung W–Cu deposit in Canada
482 (1590 ± 930 ppm; Adlakha et al. 2018), and even lower than apatite from an oxidized
483 hydrothermal system at the Xindigou orogenic Au deposit in North China (216 ± 77 ppm;
484 Zhang et al. 2020). This confirms the oxidized skarn system at the BA zone, as evidenced
485 by abundant Fe^{3+}-rich garnet (Chen et al. 2021b), diopside, magnetite, and epidote in the
486 skarns. Tin is dominantly transported as Sn^{2+}-Cl complexes under reduced conditions,
487 and cassiterite precipitation is redox- and pH-dependent (Jackson and Helgeson 1985;
488 Lehmann 1990, 2021; Taylor and Wall 1993). At the HM zone, interaction of the reduced
489 and acid Sn-bearing magmatic fluid with the late-phase granite results in the greisen-style
490 mineralization, where destruction of feldspar leads to the increase in pH of the fluid
491 system (Heinrich 1990; Lehmann 1990, 2021). At the BA zone, on the contrary, both
492 interaction of the reduced magmatic fluid with carbonate wall rocks and mixing with
493 oxidized meteoric water can lead to an increase in oxygen fugacity, as well as acid

494 neutralization (Heinrich 1990; Lehmann 1990, 2021), which triggered formation of the
495 tin skarns.
496
497 **Implications**
498 The consistent B isotopic compositions of Tur-5 from an open skarn system with
499 Tur-1 to Tur-3 from a closed magmatic-hydrothermal greisen environment (Fig. 8a)
500 suggests that tourmaline B isotopes by themselves are ineffective in discriminating the
501 entrainment of the B-poor, wall rock-derived fluids in granite-related tin deposits. In this
502 case, combination with hydrothermal apatite Sr–Nd isotopes can provide further
503 constraints on fluid sources. The similarity in Sr isotopic compositions between the
504 skarn-hosted Ap-I to Ap-III and carbonate wall rocks (Fig. 10a) indicates extensive
505 exchange between the magmatic fluid and wall rocks, and/or addition of wall
506 rock-derived meteoric water. In addition, the tourmaline and apatite compositions
507 indicate that the ore-forming magmatic fluid had high B, Na, Li, Zn, and Sn, and low Sr
508 concentrations (Table 1), which are in good agreement with previous fluid-inclusion
509 analyses and estimations by mica chemistry. During the fluid-rock interaction and
510 incursion of meteoric water, the host rocks contributed considerable amounts of Ca, Mg,
511 V, Ni, and Sr to the ore-forming system. This study also suggests that tourmaline and
512 apatite have great potential with respect to fingerprinting the oxygen fugacity conditions
513 of ore-forming fluids (Figs. 6d–6e). Thus, the textures, paragenesis, in situ elemental

514 compositions, and B–Sr–Nd isotopes of coupled tourmaline and apatite can provide more
515 accurate constraints on the nature of the fluids and associated ore-forming processes in
516 granite-related ore systems.
517
518 **Acknowledgements**

519 We are grateful to Xu-Feng Tian for his help in sampling and field survey, to Xin-Fu
520 Zhao, Jian-Hui Su for their help in taking CL images, and to Zhen-Yu Chen, Xiao-Dan
521 Chen, Xiao-Hong Mao and Ke-Jun Hou, Qian Wang for their assistance in the
522 tourmaline/apatite major-, trace-elemental, and B−Nd−Sr isotopic analyses. Daniel
523 Harlov is thanked for editorial handling and polishment, and Shun-Da Yuan and Darrell
524 Henry are appreciated for their thought-provoking comments. This research was
525 supported financially by the National Key Research and Development Program of China
526 (2018YFC0603901).
527
528 **References cited**

529 Adlakha, E., Hanley, K., Falck, H., and Boucher, B. (2018) The origin of mineralizing
530 hydrothermal fluids recorded in apatite chemistry at the Cantung W-Cu deposit,
531 NWT, Canada. European Journal of Mineralogy, 30, 1095–1113.
532 Andersson, S.S., Wagner, T., Jonsson, E., Fusswinkel, T., and Whitehose, M.J. (2019)
533 Apatite as a tracer of the source, chemistry and evolution of ore-forming fluids: The

case of the Olserum-Djupedal REE-phosphate mineralization, SE Sweden. Geochimica et Cosmochimica Acta, 255, 163–187.

Audétat, A., Günther, D., and Heinrich, C.A. (2000a) Causes for large-scale metal zonation around mineralized plutons: Fluid inclusion LA-ICP-MS evidence from the Mole granite, Australia. Economic Geology, 95, 1563–1581.

Audétat, A., Günther, D., and Heinrich, C.A. (2000b) Magmatic-hydrothermal evolution in a fractionating granite: A microchemical study of the Sn-W-F-mineralized Mole Granite (Australia). Geochemica et Cosmochimica Acta, 95, 1563–1581.

Belousova, E.A., Griffin, W.L., O'Reilly, S.Y., and Fisher, N.I. (2002) Apatite as an indicator mineral for mineral exploration: trace-element compositions and their relationship to host rock type. Journal of Geochemical Exploration, 76, 45–69.

Cao, M.J., Li, G.M., Qin, K.Z., Seitmuratova, E.Y., and Liu, Y.S. (2011) Major and trace element characteristics of apatites in granitoids from central Kazakhstan: Implications for petrogenesis and mineralization. Resource Geology, 62, 63–83.

Cao, M.J., Evans, N.J., Hollings, P., Cooke, D.R., McInnes, B.I.A., and Qin, K.Z. (2021) Apatite texture, composition, and O-Sr-Nd isotope signatures record magmatic and hydrothermal fluid characteristics at the Black Mountain porphyry deposit, Philippines. Economic Geology, 116, 1189–1207.

Chen, S.C., Yu, J.J., and Bi, M.F. (2021a) Extraction of fractionated interstitial melt from a crystal mush system generating the Late Jurassic high-silica granites from the

554 Qitianling composite pluton, South China: implications for greisen-type tin
555 mineralization. Lithos, 382–383, 105952.
556 Chen, S.C., Yu, J.J., Bi, M.F., and Lehmann, B. (2021b) Tin-bearing minerals at the
557 Furong tin deposit, South China: Implications for tin mineralization. Geochemistry,
558 in press, 125856.
559 Chu, M.F., Wang, K.L., Griffin, W.L., Chung, S.L., O'Reilly, S.Y., Pearson, N.J., and
560 Iizuka, Y. (2009) Apatite compositions: tracing petrogenetic processes in
561 Transhimalayan granitoids. Journal of Petrology, 50, 1829–1855.
562 Codeço, M.S., Weis, P., Trumbull, R.B., Hinsberg, V.V., Pinto, F., Lecumberri-Sanchez,
563 and Schleicher, A.M. (2021) The imprint of hydrothermal fluids on trace-element
564 contents in white-mica and tourmaline from the Panasqueira W-Sn-Cu deposit,
565 Portugal. Mineralium Deposita, 56, 481–508.
566 Duchoslav, M., Marks, M.A.W., Drost, K., McCammon, C., Marschall, H.R., Wenzel, T.,
567 and Markl, G. (2017) Changes in tourmaline composition during magmatic and
568 hydrothermal processes leading to tin-ore deposition: the Cornubian Batholith, SW
569 England. Ore Geology Reviews, 83, 215–234.
570 Dutrow, B.L., and Henry, D.J. (2018) Tourmaline compositions and textures: reflections
571 of the fluid phase. Journal of Geosciences, 63, 99–110.
572 Fujimaki, H. (1986) Partition-coefficients of Hf, Zr, and REE between zircon, apatite, and
573 liquid. Contributions to Mineralogy and Petrology, 94, 42–45.

574 Gilder, S.A., Gill, J., Coe, R.S., Zhao, X.X., Liu, Z.W., Wang, G.X., Yuan, K.R., Liu,
575 W.L., Kuang, G.D., and Wu, H.R. (1996) Isotopic and Paleomagnetic constraints on
576 Mesozoic tectonic evolution of south China. Journal of Geophysical Research, 101,
577 16137–16145.

578 Harlaux, M., Kouzmanov, K., Gialli, S., Laurent, O., Rielli, A., Dini, A., Chauvet, A.,
579 Menzies, A., Kalinaj, M., and Fontboté, L. (2020) Tourmaline as a tracer of
580 late-magmatic to hydrothermal fluid evolution: The world-class San Rafael tin
581 (-copper) deposit, Peru. Economic Geology, 115, 1665–1697.

582 Harlaux, M., Kouzmanov, K., Gialli, S., Marger, K., Bouvier, A., Baumgartner, L.P.,
583 Rielli, A., Dini, A., Chauvet, A., Kalinaj, M., and Fontboté, L. (2021) Fluid mixing
584 as primary trigger for cassiterite deposition: evidence from in situ $\delta^{18}O$-$\delta^{11}B$ analysis
585 of tourmaline from the world-class San Rafael tin (-copper) deposit, Peru. Earth and
586 Planetary Science Letters, 563, 116889.

587 Harlov, D.E. (2015) Apatite: A fingerprint for metasomatic processes. Elements, 11,
588 171–176.

589 Heinrich, C.A. (1990) The chemistry of hydrothermal tin (-tungsten) ore deposition.
590 Economic Geology, 85, 457–481.

591 Henry, D.J., and Guidotti, C.V. (1985) Tourmaline as a petrogenetic indicator mineral: an
592 example from the staurolite-grade metapelites of NW Maine. American Mineralogist,
593 70, 1–15.

Henry, D.J., Novák, M., Hawthorne, F.C., Ertl, A., Dutrow, B.L., Uher, P., and Pezzotta, F. (2011) Nomenclature of the tourmaline-supergroup minerals. American Mineralogist, 96, 895–913.

Henry, D.J., and Dutrow, B.L. (2011) The incorporation of fluorine in tourmaline: Internal crystallographic controls or external environmental influences? Canadian Mineralogist, 49, 41–56.

Henry, D.J., and Dutrow, B.L. (2012) Tourmaline at diagenetic to low-grade metamorphic conditions: its petrologic applicability. Lithos, 154, 16–32.

Hong, W., Cooke, D.R., Zhang, L.J., Fox, N., and Thompson, J. (2017) Tourmaline-rich features in the Heemskirk and Pieman Heads granites from western Tasmania, Australia: Characteristics, origins, and implications for tin mineralization. American Mineralogist, 102, 876–899.

Huang, F.F., Scaillet, B., Wang, R.C., Erdmann, S., Chen, Y., Faure, M., Liu, H.S., Xie, L., Wang, B., and Zhu, J.C. (2019) Experimental constraints on intensive crystallization parameters and fractionation in A-type granites: A case study on the Qitianling pluton, South China. Journal of Geophysical Research: Solid Earth, 124, 10132–10152.

Iveson, A., Webster, J.D., Rowe, M.C., and Neill, O.K. (2019) Fluid-melt trace-element partitioning behaviour between evolved melts and aqueous fluids: Experimental constraints on the magmatic-hydrothermal transport of metals. Chemical Geology,

516, 18–41.

Jackson, K.J., and Helgeson, H.C. (1985) Chemical and thermodynamic constraints on the hydrothermal transport and deposition of tin: II. Interpretation of phase relations in the Southeast Asian tin belt. Economic Geology, 80, 1365–1378.

Jiang, S.Y., Palmer, M.R., Slack, J.F., and Shaw, D.R. (1999) Boron isotope systematics of tourmaline formation in the Sullivan Pb–Zn–Ag deposit, British Columbia, Canada. Chemical Geology, 158, 131–144.

Jiang, S.Y., Yu, J.M., and Lu, J.J. (2004) Trace and rare-earth element geochemistry in tourmaline and cassiterite from the Yunlong tin deposit, Yunnan, China: implication for migmatitic–hydrothermal fluid evolution and ore genesis. Chemical Geology, 209, 193– 213

Keppler, H. (1996) Constraints from partitioning experiments on composition of subduction-zone fluids. Nature, 380, 237–240.

Legros, H., Marignac, C., Tababy, T., Mercadier, J., Richard, A., Cuney, M., Wang, R.C., Charles, N., and Lespinasse, M.Y. (2018) The ore-forming magmat-ic-hydrothermal system of the Piaotang W-Sn deposit (Jiangxi, China) as seen from Li-mica geochemistry. American Mineralogist, 103, 39–54.

Lehmann, B. (1990) Metallogeny of Tin. Lecture Notes in Earth Sciences, 218 p. Springer, Berlin.

Lehmann, B. (2021) Formation of tin ore deposits: A reassessment. Lithos, 402–403,

105756.

Li, H., Palinkas, L., Watanabe, K., and Xi, X. (2018) Petrogenesis of Jurassic A-type granites associated with Cu–Mo and W–Sn deposits in the central Nanling region, South China: Relation to mantle upwelling and intra-continental extension. Ore Geology Reviews, 92, 449–462.

Li, X.H., Li, W.X., Li, Z.X., Lo, C.H., Wang, J., Ye, M.F., Yang, Y.H. (2009) Amalgamation between the Yangtze and Cathaysia Blocks in South China: Constraints from SHRIMP U–Pb zircon ages, geochemistry and Nd–Hf isotopes of the Shuangxiwu volcanic rocks. Precambrian Res., 174, 117–128.

Mao, J.W., Li, X.F., Chen, W., Lan, X.M., and Wei, S.L. (2004) Geological characteristics of the Furong tin orefield, Hunan, ^{40}Ar-^{39}Ar dating of tin ores and related granite and its geodynamic significance for rock and ore formation. Acta Geologica Sinica - English Edition, 78, 481–491.

Mao, J.W., Cheng, Y.B., Chen, M.H., and Pirajno, F. (2013) Major types and time–space distribution of Mesozoic ore deposits in South China and their geodynamic settings. Mineralium Deposita, 48, 267–294.

Marschall, H.R., Meyer, C., Wunder, B., Ludwig, T., and Heinrich, W. (2009) Experimental boron isotope fractionation between tourmaline and fluid: confirmation from in situ analyses by secondary ion mass spectrometry and from Rayleigh fractionation modelling. Contributions to Mineralogy and Petrology, 158,

675–681.

Marschall, H.R., and Jiang, S.Y. (2011) Tourmaline isotopes: no element left behind. Elements, 7, 313–319.

Meyer, C., Wunder, B., Meixner, A., Romer, and Heinrich, W. (2008) Boron-isotope fractionation between tourmaline and fluid: an experimental re-investigation. Contributions to Mineralogy and Petrology, 156, 259–267.

Miles, A., Graham, C., Hawkesworth, C., Gillespie, M., Hinton, R., and Bromiley, G. (2014) Apatite: a new redox proxy for silicic magmas? Geochimica et Cosmochimica Acta, 132, 101–119.

Mohamed, F.H., Abdalla, H.M., and Helba, H. (1999) Chemistry of micas in rare-metal granitoids and associated rocks, Eastern Dessert, Egypt. International Geology Review, 41, 932–948.

Müller, B., Frischknecht, R., Seward, T.M., Heinrich, C.A., and Gallegos, W.C. (2001) A fluid inclusion reconnaissance study of the Huanuni tin deposit (Belivia), using LA-ICP-MS micro-analysis. Mineralium Deposita, 36, 680–688.

O'Sullivan, G., Chew, D., Kenny, G., Henrichs, I., and Mulligan, D. (2020) The trace element composition of apatite and its application to detrital provenance studies. Earth-Science Reviews, 201, 103044.

Pennisi, M., Leeman, W.P., Tornarini, S., Pennisi, A., and Nabelek, P. (2000) Boron, Sr, O, and H isotope geochemistry of groundwaters from Mt. Etna (Sicily) – hydrologica

674 implications. Geochimica et Cosmochimica Acta, 64, 961–974.
675 Pesquera, A., Torres-Ruiz, J., Garcia-Casco, A., Gil-Crespo, P.P. (2013) Evaluating the
676 controls on tourmaline formation in granitic systems: a case study on peraluminous
677 granites from the Central Iberian Zone (CIZ), Western Spain. Journal of Petrology,
678 54, 609–634.
679 Qiu, KF., Yu, H.C., Hetherington, C., Huang, Y.Q., Yang, T., and Deng, J. (2021)
680 Tourmaline composition and boron isotope signature as a tracer of
681 magmatic-hydrothermal processes. American Mineralogist, 106, 1033–1044.
682 Schmidt, C., Romer, R.L., Wohlgemuth-Ueberwasser, C.C., and Appelt, O. (2020)
683 Partitioning of Sn and W between granitic melt and aqueous fluid. Ore Geology
684 Reviews, 117, 103263.
685 Sha, L.K., and Chappell, B.W. (1999) Apatite chemical composition, determined by
686 electron microprobe and lase-ablation inductively coupled plasma mass
687 spectrometry, as a probe into granite petrogenesis. Geochimica et Cosmochimica
688 Acta, 63, 3861–3881.
689 Sheppard, S.M.F. (1986) Characterization and isotopic variations in natural waters.
690 Reviews in Mineralogy and Geochemistry, 16, 165–183.
691 Shuang, Y., Bi, X.W., Hu, R.Z., Peng, J.T., Su, W.C., and Zhu, C.S. (2009) Study on the
692 ore-forming fluid geochemistry of the Furong tin polymetallic deposit, Hunan
693 Province, China. Acta Petrologica Sinica, 25, 2588–2600. (in Chinese with English

694 abstract)

695 Slack, J.F., and Trumbull, R.B. (2011) Tourmaline as a recorder of ore-forming process.
696 Elements, 7, 321–326.

697 South Hunan Geological Survey. (2005) Mineral exploration report of the Bailashui tin
698 mine in Chenzhou city, Hunan Province. (unpublished report in Chinese).

699 Su, Z.K., Zhao, X.F., Li, X.C., and Zhou, M.F. (2016) Using elemental and boron isotopic
700 compositions of tourmaline to trace fluid evolutions of IOCG systems: The
701 worldclass Dahongshan Fe–Cu deposit in SW China. Chemical Geology, 441,
702 265–279.

703 Sun, S.S., and Mcdonough, W.F. (1989) Chemical and isotopic systematics of oceanic
704 basalts: implications for mantle composition and processes. Geological Society
705 London Special Publications, 42, 313–345.

706 Taylor, J.R., and Wall, V.J. (1993) Cassiterite solubility, tin speciation, and transport in a
707 magmatic aqueous phase. Economic Geology, 88, 437–460.

708 Trumbull, R.B., Codeço, M.S., Jiang, S.Y., Palmer, M.R., and Slack, J.F. (2020) Boron
709 isotope variations in tourmaline from hydrothermal ore deposits: A review of
710 controlling factors and insights for mineralizing systems. Ore Geology Reviews, 125,
711 103682.

712 van Hinsberg, V.J. (2011) Preliminary experimental data on trace-element partitioning
713 between tourmaline and silicate melt. The Canadian Mineralogist, 49, 153–163.

van Hinsberg, V.J., Franz, G., and Wood, B.J. (2017) Determining subduction-zone fluid composition using a tourmaline mineral probe. Geochemical Perspectives Letters, 3, 160–169.

Wang, Y.J., Fan, W.M., Zhang, G.W., and Zhang, Y.H. (2013) Phanerozoic tectonics of the South China Block: Key observations and controversies. Gondwana Research, 23, 1273–1305.

Wang, Z.Q., Chen, B., and Ma, X.H. (2014) In situ LA–ICP–MS U–Pb age and geochemical data of cassiterite of the Furong tin deposit, the Nanling Range: Implications for the origin and evolution of the ore-forming fluid. Chinese Science Bulletin (Chinese Version), 59, 2505–2519. (in Chinese)

Wolf, M.B., and London, D. (1997) Boron in granitic magmas: stability of tourmaline in equilibrium with biotite and cordierite. Contributions to Mineralogy and Petrology, 130, 12–30.

Xu, R., Romer, R.L., and Glodny, J. (2021) External fluids cause alteration and metal redistribution in the granite-hosted Tangziwa Sn–Cu deposit, Gejiu district, China: Lithos, 382–383, 105937.

Yan, J.X., and Wu, M. (2004) Strontium isotope and its geological implications of chrysanthemum-shaped celestite of the Qixia formation of Permian in South China. Journal of Palaeogeography, 6, 191–195. (in Chinese with English abstract)

Yang, S.Y., Jiang, S.Y., Zhao, K.D., Dai, B.Z., and Yang, T. (2015) Tourmaline as a

734 recorder of magmatic–hydrothermal evolution: an in situ major and trace element
735 analysis of tourmaline from the Qitianling batholith, South China. Contributions to
736 Mineralogy and Petrology, 170, 42.
737 Yuan, S.D., Peng, J.T., Hu, R.Z., Bi, X.W., Qi, L., Li. Z.L., Li, X.M., and Shuang, Y.
738 (2008) Characteristics of rare-earth elements (REE), strontium and neodymium
739 isotopes in hydrothermal fluorites from the Bailashui tin deposit in the Furong ore
740 field, southern Hunan Province, China. Chinese Journal of Geochemistry, 27,
741 342–350.
742 Yuan, S.D., Peng, J.T., Hao, S., Li, H.M., Geng, J.Z., and Zhang, D.L. (2011) In situ
743 LA-MC-ICP-MS and ID-TIMS U-Pb geochronology of cassiterite in the giant
744 Furong tin deposit, Hunan Province, South China: New constraints on the timing of
745 tin–polymetallic mineralization. Ore Geology Reviews, 43, 235–242.
746 Yuan, S.D., Williams-Jones, A.E., Romer, R.L., Zhao, P.L., and Mao, J.W. (2019)
747 Photolith-related thermal controls on the decoupling of Sn and W in Sn–W
748 metallogenic provinces: Insights from the Nanling Region, China. Economic
749 Geology, 114, 1005–1012.
750 Zajacz, Z., Halter, W.E., Pettke, T., and Guillong, M. (2008) Determination of fluid/melt
751 partition coefficients by LA-ICPMS analysis of co-existing fluid and silicate melt
752 inclusions: controls on element partitioning. Geochemica et Cosmochimica Acta, 72,
753 2169–2197.

754 Zeng, L.P., Zhao, X.F., Li, X.C., Hu, H., and McFarlane, C. (2016) In situ elemental and
755 isotopic analysis of fluorapatite from the Taocun magnetite-apatite deposit, Eastern
756 China: Constraints on fluid metasomatism. American Mineralogist, 101, 2468–2483.
757 Zhang, F.H., Li, W.B., White, N.C., Zhang, L.J., Qiao, X.Y., and Yao, Z.W. (2020)
758 Geochemical and isotopic study of metasomatic apatite: Implications for gold
759 mineralization in Xindigou, Northern China. Ore Geology Reviews, 127, 103853.
760 Zhao, K.D., Jiang, S.Y., Nakamura, E., Moriguti, T., Palmer, M.R., Yang, S.Y., Dai, B.Z.,
761 and Jiang, Y.H. (2011) Fluid–rock interaction in the Qitianling granite and
762 associated tin deposits, South China: Evidence from boron and oxygen isotopes. Ore
763 Geology Reviews, 43, 243–248.
764 Zhao, K.D., Jiang, S.Y., Yang, S.Y., Dai, B.Z., and Lu, J.J. (2012) Mineral chemistry,
765 trace elements and Sr–Nd–Hf isotope geochemistry and petrogenesis of Cailing and
766 Furong granites and mafic enclaves from the Qitianling batholith in the Shi-Hang
767 zone, South China. Gondwana Research, 22, 310–324.
768 Zhao, P.L., Zajacz, Z., Tsay, A., and Yuan, S.D. (2021) Magmatic-hydrothermal tin
769 deposits form in response to efficient tin extraction upon magma degassing.
770 Geochimica et Cosmochimica Acta, in press.
771 Zhao, X.F., Zhou, M.F., Gao, J.F., Li, X.C., and Li, J.W. (2015) In situ Sr isotope analysis
772 of apatite by LA-MC-ICPMS: Constraints on the evolution of ore-fluids of the
773 Yinachang Fe-Cu-REE deposit, Southwest China. Mineralium Deposita, 50,

871–884.

Zhu, J.C., Wang, R.C., Zhang, P.H., Xie, C.F., Zhang, W.L., Zhao, K.D., Xie, L., Yang, C., Che, X.D., Yu, A.P., and Wang, L.B. (2009) Zircon U–Pb geochronological framework of Qitianling granite batholith, middle part of Nanling Range, South China. Science China: Earth Science, 52, 1279–1294.

780

781 ## Figure Captions

782 **Figure 1.** (**a**) Main tectonic units of South China (Wang et al. 2013). (**b**) Geological
783 map of the Nanling Range, showing the distribution of granites and associated W–Sn
784 deposits (Yuan et al. 2019). (**c**) Geological map of the Furong deposit (Yuan et al. 2011).

785 **Figure 2.** Geological map of the Bailashui-Anyuan zone at Furong (modified from
786 South Hunan Geological Survey 2005).

787 **Figure 3.** Photographs and microphotographs of tourmaline in the late-phase granite
788 (a, b), nodule (c−h), vein (i−k), and greisen-type ore (l−o) at the HM zone. (**a**) Tur-1
789 occurs interstitial to quartz, K-feldspar, and albite (plane-polarized light). (**b**) Tur-1 in Fig.
790 3a is homogeneous in BSE image. (**c**) Quartz-tourmaline nodule is rimmed by a
791 leucocratic halo. (**d**) Nodular Tur-1 co-exists with quartz and albite (plane-polarized
792 light). (**e**) Brown Tur-1 is replaced by blue Tur-2 and fluorite (plane-polarized light). (**f**)
793 Tur-1 in Fig. 3e is replaced by Tur-2 with visible voids and fluorite inclusions in BSE
794 image. (**g**) Albite is replaced by muscovite (cross-polarized light). (**h**) Nodular Tur-2 are
795 included by or intergrown with arsenopyrite (plane-polarized light). (**i**) Quartz-Tur-2 vein
796 crosscuts the late-phase granite and quartz-tourmaline nodule. (**j**) Vein-type Tur-2 shows
797 orange to yellow-green and blue pleochroism (plane-polarized light). (**k**) Vein-type Tur-2
798 has weak patchy zoning in BSE image. (**l**) Tur-3 co-exists with quartz, muscovite, and
799 cassiterite (plane-polarized light). (**m**) Tur-3 in Fig. 3l shows weak oscillatory zoning in

BSE image. (**n**) Tur-3 co-exists with arsenopyrite and quartz (plane-polarized light). (**o**) Tur-3 co-existing with chalcopyrite is homogeneous in BSE image. Ab = albite, Apy = arsenopyrite, Ccp = Chalcopyrite, Cst = cassiterite, Fl = fluorite, Kfs = K-feldspar, Ms = muscovite, Qz = quartz, Tur = tourmaline.

Figure 4. Photographs and microphotographs of tourmaline in the vein crosscutting the main-phase granite (a–e) and skarn-type ore (f, g) at the BA zone. (**a**) Quartz-Tur-4 vein rimmed by leucocratic halos crosscuts the main-phase granite. (**b**) Tur-4 occurs mainly as radiating, coarse-grained, euhedral prismatic crystals (plane-polarized light). (**c**) Tur-4 in Fig. 4b shows weak oscillatory zoning in BSE image. (**d-e**) Tur-4 is locally intergrown with or replaced by muscovite and sphalerite (plane-polarized light). (**f**) Vesuvianite is replaced by Tur-5, pargasite, fluorite and cassiterite (cross-polarized light). (**g**) Tur-5 in Fig. 4f shows patchy zoning in BSE image. Prg = pargasite, Ves = vesuvianite. Other mineral abbreviations as in Fig. 3.

Figure 5. Microphotographs of apatite in the main-phase granite (a–c) and in the skarn (d–i) and skarn-type ore (j–o) at the BA zone. (**a**) Ap-G is mainly included by biotite (plane-polarized light). (**b**) Ap-G in Fig. 5a displays yellow-green to light green luminescence in CL image. (**c**) Ap-G in Fig. 5b is homogeneous and bright in BSE image. (**d**) Ap-I is included by garnet (plane-polarized light). (**e**) Ap-I in Fig. 5d displays blue luminescence with very narrow green rims in CL image. (**f**) Ap-I in Fig. 5e is homogeneous in BSE image. (**g**) Apatite is interstitial between diopside grains

(plane-polarized light). (**h**) Apatite in Fig. 5g displays color zoning with blue cores (Ap-I) and green rims (Ap-II) in CL image. (**i**) Apatite in Fig. 5h consists of light grey cores (Ap-I) and dark grey rims (Ap-II) in BSE image. (**j**) Ap-II veinlet occurs in the skarn-type ore (plane-polarized light). (**k**) Ap-II in Fig. 5j consists of very small blue cores and green rims in CL image. (**l**) The core-rim texture of Ap-II in Fig. 5k is very weak in high-contrast BSE image. (**m**) Ap-III co-exists with sphalerite (plane-polarized light). (**n**) Ap-III in Fig. 5m shows color zoning with light bluish grey cores and green rims in CL image. (**o**) Ap-III in Fig. 5n is homogeneous in BSE image. Ap = apatite, Bt = biotite, Di = diopside, Grt = garnet, Ilm = ilmenite, Sp = sphalerite. Other mineral abbreviations as in Figs. 3 and 4.

Figure 6. Compositional variations of the Furong tourmaline. (**a**) Ca–$X_{□}$–(Na+K) ternary diagram (Henry et al. 2011). (**b**) Fe/(Fe+Mg) vs. $X_{□}/(X_{□}+Na+K)$ (Henry and Guidotti 1985), (**c**) Mg vs. Fe, (**d**) Al vs. Fe, and (**e**) Al vs. $X_{□}$ binary diagrams. Fe/(Fe+Mg) vs. F(**f**), Li (**g**), V (**h**), Ni (**i**), Sr (**j**), Zn (**k**), and Sn (**l**) binary diagrams.

Figure 7. (**a**) MgO, (**b**) F, (**c**) Li, (**d**) Sc, (**e**) Zn, and (**f**) Sn for Tur-1 vs. corresponding Tur-2 from individual crystals within tourmaline nodules.

Figure 8. (**a**) Histogram of B isotopic compositions of the Furong tourmaline. N is the number of analyses. (**b**) $\delta^{11}B$ values for Tur-1 vs. corresponding Tur-2 from individual crystals within tourmaline nodules.

Figure 9. (**a**) Fe vs. V, (**b**) Mn vs. Sr (Belousova et al. 2002), (**c**) Y vs, Sr

(Belousova et al. 2002), (**d**) Ga vs. (Th+U), (**e**) Na vs. REE, and (**f**) LREE vs. Sr/Y (O'Sullivan et al. 2020) binary diagrams for the Furong apatite. ALK = alkali-rich igneous rocks, IM = mafic I-type granitoids and mafic igneous rocks, LM = low- and medium-grade metamorphic and hydrothermal altered rocks, HM = partial-melts/leucosomes/high-grade metamorphic, S = S-type granitoids and high A/CNK 'felsic' I-types, UM = ultramafic rocks including carbonatites, lherzolites and pyroxenites.

Figure 10. Chondrite-normalized REE patterns of (**a**) Ap-G, (**b**) Ap-I, and (**c**) Ap-II and Ap-III at Furong. The whole-rock REE data for the main-phase granite and Permian carbonate wall rocks are from Zhao et al. (2012) and Wang et al. (2014), respectively. Chondrite values used for normalization are from Sun and McDonough (1989).

Figure 11. (**a**) Sr isotopic compositions and (**b**) T_{DM2} vs. $\varepsilon_{Nd(t)}$ diagram of the Furong apatite. Data for the Permian carbonate rocks are from Yan and Wu (2014), data for the Qitianling granites from Zhao et al. (2012) and Chen et al. (2021a), and data for fluorite from Yuan et al. (2011).

Figure 12. (**a**) Comparison of B isotopic data from Furong with major boron reservoirs and tourmaline from different environments (Marschall and Jiang 2011). (**b**) Variations in calculated $\delta^{11}B_{fluid}$ values at Furong, and Rayleigh fractionation model on B isotopic evolution of the fluid during tourmaline precipitation. The whole-rock $\delta^{11}B$ values for the Qitianling granites are from Zhao et al. (2011).

Appendix

Appendix 1. Paragenetic sequence of alteration minerals and mineralization at the greisen-type HM zone (**a**) and skarn-type No. 19 orebody at the BA zone (**b**).

Appendix 2. Analytical methods and calculation method of tourmaline–fluid partition coefficients.

Appendix 3. Major- and trace-elemental composition of the Furong tourmaline.

Appendix 4. Boron isotope composition of the Furong tourmaline.

Appendix 5. Major- and trace-elemental composition of the Furong apatite.

Appendix 6. Sr–Nd isotope composition of the Furong apatite.

Table 1 Summary of the average elemental composition of the Furong tourmaline.

Type	Tur-1 N=32	Tur-2 N=39	Tur-3 N=49	Tur-4 N=31	Tur-5 N=16
EPMA (wt%)					
SiO_2	34.4 (0.3)	34.4 (0.4)	35.0 (0.4)	35.5 (0.4)	33.5 (0.9)
TiO_2	0.5 (0.2)	0.2 (0.2)	0.6 (0.3)	0.5 (0.3)	0.4 (0.3)
Al_2O_3	29.9 (0.9)	30.2 (1.2)	30.4 (1.1)	32.9 (0.8)	28.5 (2.6)
FeO	17.1 (0.8)	17.2 (1.1)	15.5 (1.2)	11.9 (0.8)	16.9 (1.5)
MnO	0.1 (0)	0.1 (0)	0 (0)	0 (0)	0.1 (0)
MgO	0.3 (0.1)	0.2 (0.2)	1.0 (0.4)	2.4 (0.4)	2.0 (0.9)
CaO	0 (0)	0 (0)	0.3 (0.1)	0.5 (0.2)	1.9 (0.5)
Na_2O	2.4 (0.2)	2.4 (0.4)	2.0 (0.2)	1.5 (0.2)	1.8 (0.2)
K_2O	0.1 (0)	0.1 (0)	0 (0)	0 (0)	0 (0)
F	0.9 (0.2)	0.8 (0.3)	0.4 (0.2)	0.2 (0.1)	0.4 (0.1)
Cl	0 (0)	0 (0)	0 (0)	0 (0)	0 (0)
Total	85.7 (0.3)	85.5 (0.4)	85.3 (0.3)	85.5 (0.4)	85.3 (0.3)
Atomic proportions based on the sum of T+Z+Y cations normalized to 15 cations					
Si (apfu)	6.08 (0.04)	6.08 (0.04)	6.12 (0.04)	6.03 (0.06)	5.95 (0.16)
Al (T-site)	0 (0)	0 (0)	0 (0)	0.01 (0.03)	0.08 (0.13)
Al (Z-site)	5.99 (0.04)	6.00 (0.01)	6.00 (0.01)	6.00 (0)	5.76 (0.21)
Al (Y-site)	0.25 (0.14)	0.30 (0.20)	0.26 (0.17)	0.58 (0.14)	0.11 (0.25)
Al (total)	6.24 (0.16)	6.30 (0.20)	6.26 (0.17)	6.59 (0.15)	5.96 (0.49)
Ti	0.06 (0.03)	0.02 (0.03)	0.08 (0.04)	0.07 (0.04)	0.05 (0.05)
Fe	2.53 (0.12)	2.55 (0.18)	2.27 (0.19)	1.70 (0.12)	2.50 (0.25)
Mn	0.02 (0.01)	0.02 (0.01)	0.01 (0)	0 (0)	0.01 (0)
Mg	0.08 (0.03)	0.04 (0.05)	0.27 (0.11)	0.61 (0.11)	0.52 (0.24)
Ca	0 (0)	0.01 (0.02)	0.05 (0.02)	0.09 (0.04)	0.36 (0.1)
Na	0.84 (0.06)	0.82 (0.13)	0.67 (0.06)	0.49 (0.05)	0.60 (0.08)
K	0.01 (0)	0.01 (0.01)	0.01 (0)	0 (0)	0.01 (0)
$X_{\square}$	0.15 (0.06)	0.16 (0.13)	0.27 (0.07)	0.41 (0.05)	0.04 (0.04)
OH	3.5 (0.11)	3.55 (0.15)	3.77 (0.12)	3.90 (0.07)	3.78 (0.07)
F	0.5 (0.11)	0.45 (0.15)	0.23 (0.12)	0.09 (0.07)	0.22 (0.07)
Cl	0 (0)	0 (0)	0 (0)	0 (0)	0 (0)
Fe/(Fe+Mg)	0.97 (0.01)	0.98 (0.02)	0.89 (0.04)	0.73 (0.04)	0.83 (0.07)
LA−ICP−MS (ppm)					
Li	149 (81)	99 (46)	98 (33)	31 (14)	179 (74)
Be	19 (11)	8 (6)	11 (8)	14 (9)	26 (22)
Sc	24 (20)	14 (15)	7 (5)	16 (10)	1 (1)
V	3 (2)	1 (1)	30 (25)	111 (44)	29 (18)
Cr	4 (7)	21 (39)	34 (45)	34 (68)	18 (18)
Co	2 (3)	1 (1)	1 (1)	7 (1)	12 (5)
Ni	1 (2)	1 (2)	1 (1)	11 (4)	7 (4)

Type	Tur-1 N=32	Tur-2 N=39	Tur-3 N=49	Tur-4 N=31	Tur-5 N=16
Zn	220 (58)	198 (37)	134 (29)	89 (7)	291 (37)
Ga	124 (33)	110 (25)	129 (46)	80 (11)	34 (7)
Sr	11 (16)	4 (2)	182 (65)	159 (52)	219 (72)
Sn	107 (69)	234 (136)	177 (96)	412 (207)	435 (272)
REE (total)	25 (27)	17 (18)	12 (8)	23 (14)	38 (61)
Y	0 (0)	2 (7)	1 (4)	5 (7)	0 (0)
Na_{fluid} (wt%)	6.0 (0.4)	5.9 (0.9)	4.9 (0.9)	3.7 (0.4)	4.3 (0.6)
Li_{fluid} (ppm)	498 (269)	329 (155)	326 (111)	104 (46)	597 (248)
Zn_{fluid}	2199 (580)	1978 (366)	1342 (292)	890 (70)	2907 (372)
Sr_{fluid}	6.0 (9)	2 (1)	96 (34)	83 (27)	115 (38)

Total Fe is reported as FeO. X□ is vacancy in X-site. REE is the rare earth elements. Subscript "fluid" is the estimated element concentrations in the fluids responsible for tourmaline. Numbers in parentheses are standard deviations of the mean (1sd). N=analyzed spot numbers.

Table 2 Summary of the average elemental composition of the Furong apatite.

Type	Ap-G	Ap-I	Ap-II	Ap-III
EPMA (wt%)	N=66	N=24	N=35	N=18
P_2O_5	42.1 (0.4)	41.6 (0.6)	41.9 (0.4)	42.2 (0.6)
SiO_2	0 (0)	0 (0)	0 (0)	0 (0)
SO_3	0 (0)	0 (0)	0 (0)	0 (0)
TiO_2	0 (0)	0 (0)	0 (0)	0 (0)
Al_2O_3	0 (0)	0 (0)	0 (0)	0 (0)
FeO	0.2 (0.1)	0.1 (0)	0.1 (0.1)	0.1 (0.1)
MnO	0.1 (0)	0 (0)	0 (0)	0 (0)
MgO	0 (0)	0 (0)	0 (0)	0 (0)
CaO	54.7 (0.6)	55.4 (0.6)	55.9 (0.6)	55.8 (0.8)
BaO	0 (0)	0 (0)	0 (0)	0 (0)
Na_2O	0.1 (0)	0 (0)	0 (0)	0 (0)
K_2O	0 (0)	0 (0)	0 (0)	0 (0)
F	3.4 (0.4)	3.5 (0.4)	3.5 (0.4)	3.4 (0.3)
Cl	0.2 (0.2)	0.2 (0.1)	0.1 (0.1)	0.1 (0.2)
Total	99.3 (0.8)	99.3 (0.9)	99.9 (0.8)	100.2 (1.1)
Formula calculation based on 8 cations with F+Cl+OH = 1				
P	3.01 (0.03)	2.97 (0.03)	2.97 (0.02)	2.98 (0.03)
Si	0 (0)	0 (0)	0 (0)	0 (0)
S	0 (0)	0 (0)	0 (0)	0 (0)
Ti	0 (0)	0 (0)	0 (0)	0 (0)
Al	0 (0)	0 (0)	0 (0)	0 (0)
Fe^{2+}	0.01 (0.01)	0.01 (0)	0 (0)	0.01 (0)
Mn	0 (0)	0 (0)	0 (0)	0 (0)
Mg	0 (0)	0 (0)	0 (0)	0 (0)
Ca	4.96 (0.03)	5.01 (0.03)	5.02 (0.02)	5.00 (0.03)
Ba	0 (0)	0 (0)	0 (0)	0 (0)
Na	0.01 (0)	0 (0)	0 (0)	0 (0)
K	0 (0)	0 (0)	0 (0)	0 (0)
F	0.90 (0.11)	0.95 (0.09)	0.93 (0.10)	0.89 (0.07)
Cl	0.03 (0.02)	0.02 (0.02)	0.01 (0.01)	0.02 (0.02)
OH	0.09 (0.09)	0.06 (0.06)	0.08 (0.08)	0.10 (0.08)
LA−ICP−MS (ppm)	N=38	N=13	N=28	N=21
Na	597 (244)	266 (279)	139 (190)	126 (197)
Fe	650 (454)	298 (273)	89 (86)	157 (171)
Mn	523 (101)	111 (36)	149 (31)	124 (21)
V	5 (4)	15 (9)	25 (36)	16 (5)
Ga	11 (3)	4 (1)	1 (2)	1 (1)

Type	Ap-G	Ap-I	Ap-II	Ap-III
Rb	0 (1)	2 (2)	1 (1)	0 (0)
Sr	102 (15)	1265 (604)	1970 (898)	938 (160)
Y	1475 (383)	395 (259)	138 (202)	111 (27)
La	1170 (336)	555 (270)	179 (245)	292 (62)
Ce	3188 (868)	940 (518)	296 (445)	270 (56)
Pr	422 (109)	115 (76)	37 (61)	59 (13)
Nd	1791 (444)	448 (323)	152 (255)	230 (53)
Sm	365 (90)	84 (67)	29 (51)	35 (8)
Eu	7 (2)	13 (8)	4 (7)	6 (1)
Gd	318 (81)	76 (60)	27 (45)	25 (6)
Tb	44 (12)	11 (9)	4 (6)	3 (1)
Dy	256 (68)	59 (47)	21 (35)	16 (4)
Ho	48 (13)	11 (8)	4 (6)	3 (1)
Er	128 (33)	30 (22)	10 (17)	8 (2)
Tm	17 (4)	3 (2)	1 (2)	1 (0)
Yb	98 (27)	17 (12)	6 (9)	4 (1)
Th	24 (20)	394 (506)	213 (538)	45 (14)
U	10 (8)	199 (217)	133 (224)	59 (32)
REE (total)	7863 (2045)	2363 (1392)	770 (1183)	952 (206)
La_N/Yb_N	8.7 (1.9)	30.1 (14.3)	23.6 (5.7)	52.3 (9.2)
δEu	0.1 (0)	0.6 (0.2)	0.5 (0.2)	0.6 (0)

Total Fe is reported as FeO. REE is the rare earth elements. $\delta Eu = 2Eu_N/(Sm_N+Gd_N)$, where subscript N means normalization to chondrite (Sun and McDonough, 1989). Numbers in parentheses are standard deviations of the mean (1sd). N=analyzed spot numbers.

Figure 1

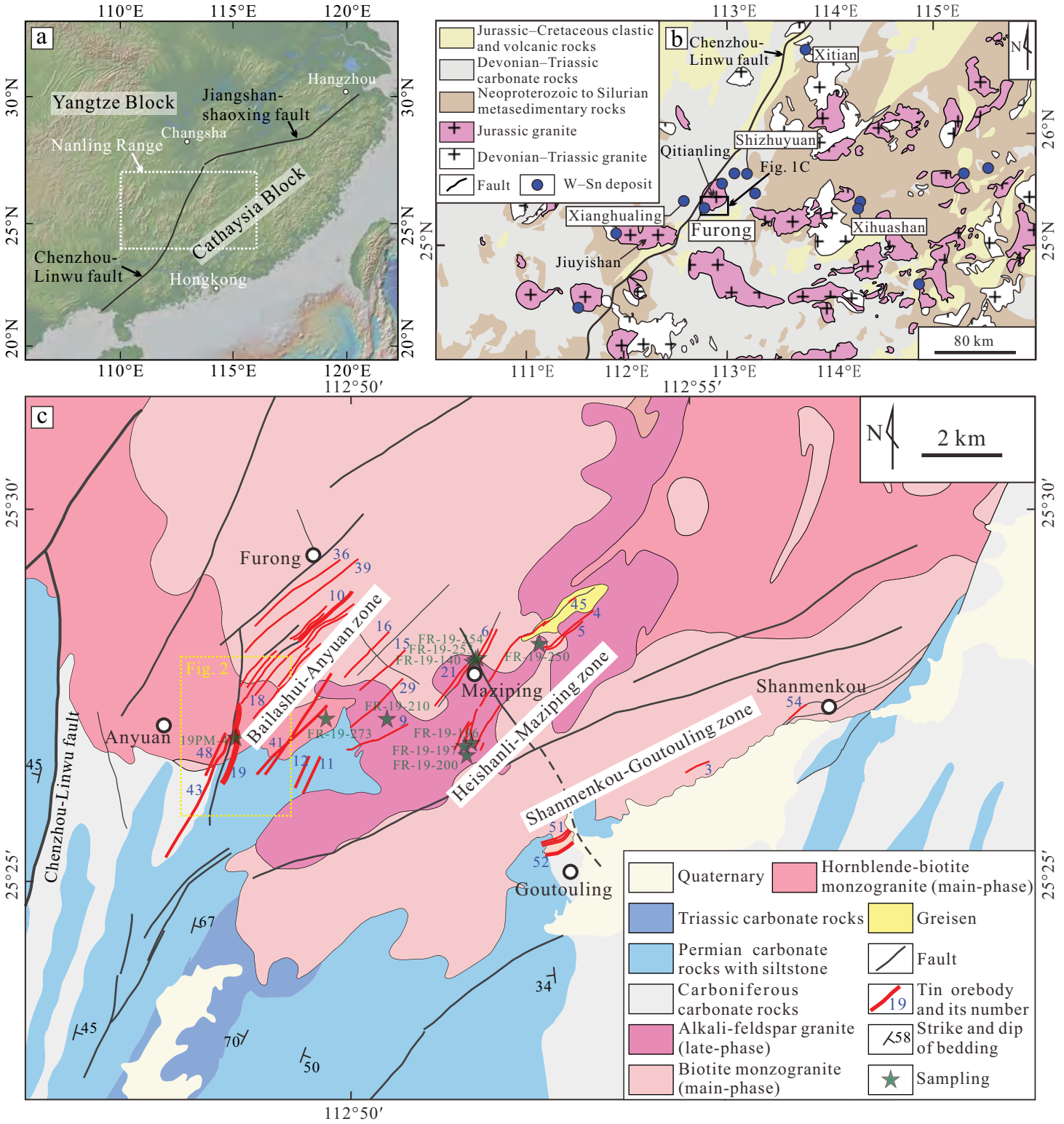
a
Yangtze Block
Jiangshan-shaoxing fault
Hangzhou
Changsha
Nanling Range
Cathaysia Block
Chenzhou-Linwu fault
Hongkong
110°E
115°E
120°E
30°N
25°N
20°N
b
Jurassic–Cretaceous clastic and volcanic rocks
Devonian–Triassic carbonate rocks
Neoproterozoic to Silurian metasedimentary rocks
Jurassic granite
Devonian–Triassic granite
Fault
W–Sn deposit
Chenzhou-Linwu fault
Xitian
Shizhuyuan
Qitianling
Fig. 1C
Xianghualing
Furong
Xihuashan
Jiuyishan
80 km
113°E
114°E
115°E
26°N
25°N
111°E
112°E
c
N
2 km
Furong
Anyuan
Maziping
Shanmenkou
Goutouling
Bailashui-Anyuan zone
Heishanli-Maziping zone
Shanmenkou-Goutouling zone
Chenzhou-Linwu fault
Fig. 2
19PM-A1
FR-19-254
FR-19-253
FR-19-140
FR-19-250
FR-19-210
FR-19-273
FR-19-196
FR-19-197
FR-19-200
112°50′
112°55′
25°30′
25°25′
Quaternary
Triassic carbonate rocks
Permian carbonate rocks with siltstone
Carboniferous carbonate rocks
Alkali-feldspar granite (late-phase)
Biotite monzogranite (main-phase)
Hornblende-biotite monzogranite (main-phase)
Greisen
Fault
Tin orebody and its number
Strike and dip of bedding
Sampling

Figure 2

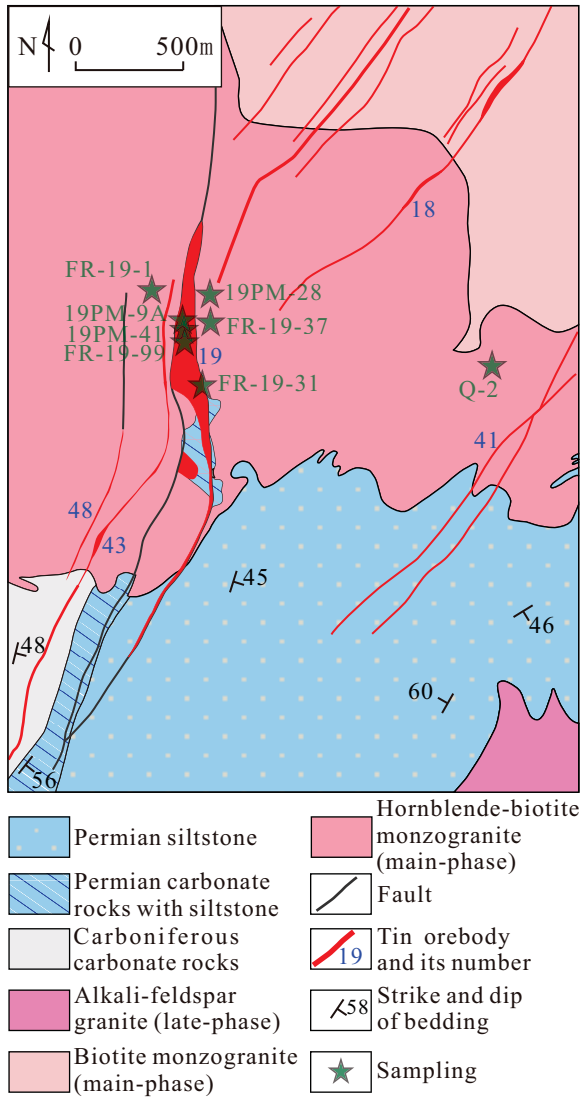
N
0
500m
18
FR-19-1
19PM-28
19PM-9A
19PM-41
FR-19-37
FR-19-99
19
FR-19-31
Q-2
41
48
43
45
46
48
60
56
Permian siltstone
Permian carbonate rocks with siltstone
Carboniferous carbonate rocks
Alkali-feldspar granite (late-phase)
Biotite monzogranite (main-phase)
Hornblende-biotite monzogranite (main-phase)
Fault
19
Tin orebody and its number
58
Strike and dip of bedding
Sampling

Figure 3

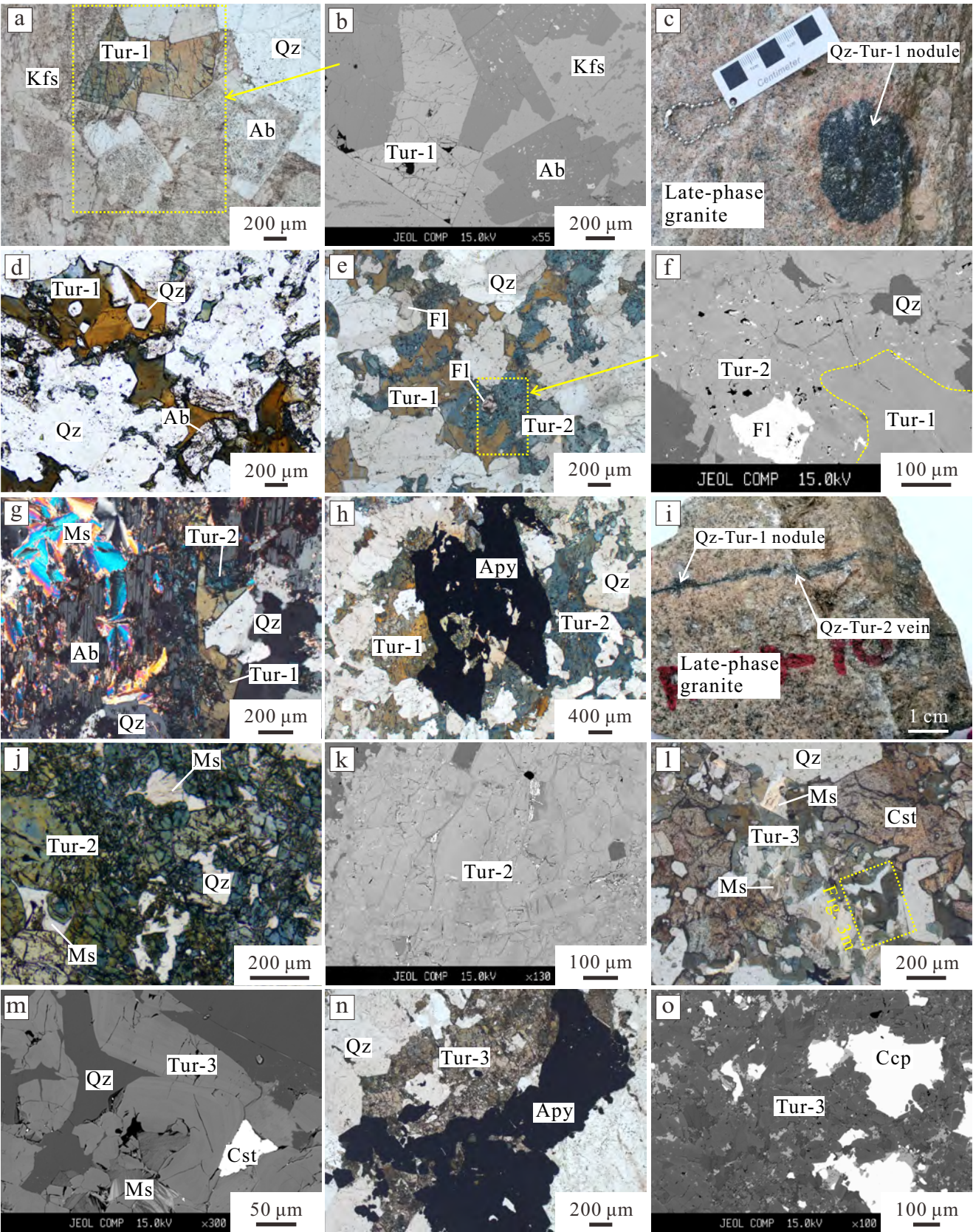
a
Tur-1
Qz
Kfs
Ab
200 μm
b
Kfs
Tur-1
Ab
JEOL COMP 15.0kV ×55
200 μm
c
Qz-Tur-1 nodule
Late-phase granite
d
Tur-1
Qz
Qz
Ab
200 μm
e
Qz
Fl
Fl
Tur-1
Tur-2
200 μm
f
Qz
Tur-2
Fl
Tur-1
JEOL COMP 15.0kV
100 μm
g
Ms
Tur-2
Qz
Ab
Tur-1
Qz
200 μm
h
Apy
Qz
Tur-2
Tur-1
400 μm
i
Qz-Tur-1 nodule
Qz-Tur-2 vein
Late-phase granite
1 cm
j
Ms
Tur-2
Qz
Ms
200 μm
k
Tur-2
JEOL COMP 15.0kV ×130
100 μm
l
Qz
Ms
Cst
Tur-3
Ms
Fig. 3m
200 μm
m
Qz
Tur-3
Cst
Ms
JEOL COMP 15.0kV ×300
50 μm
n
Qz
Tur-3
Apy
200 μm
o
Ccp
Tur-3
JEOL COMP 15.0kV ×100
100 μm

Figure 4

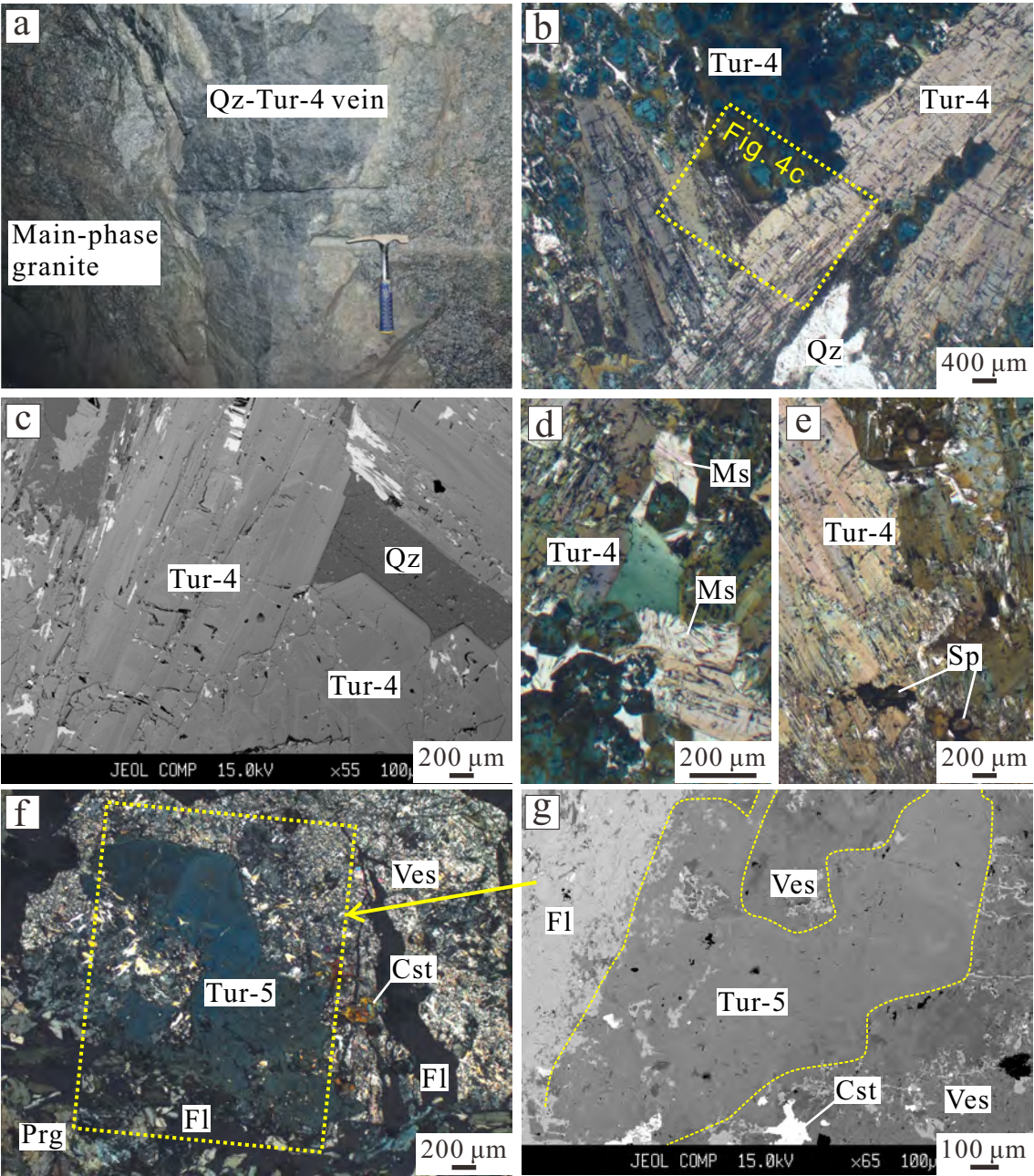
a
Qz-Tur-4 vein
Main-phase granite
b
Tur-4
Tur-4
Fig. 4c
Qz
400 μm
c
Tur-4
Qz
Tur-4
JEOL COMP 15.0kV ×55 100μ
200 μm
d
Ms
Tur-4
Ms
200 μm
e
Tur-4
Sp
200 μm
f
Ves
Cst
Tur-5
Fl
Fl
Prg
200 μm
g
Ves
Fl
Tur-5
Cst
Ves
JEOL COMP 15.0kV ×65 100μ
100 μm

Figure 5

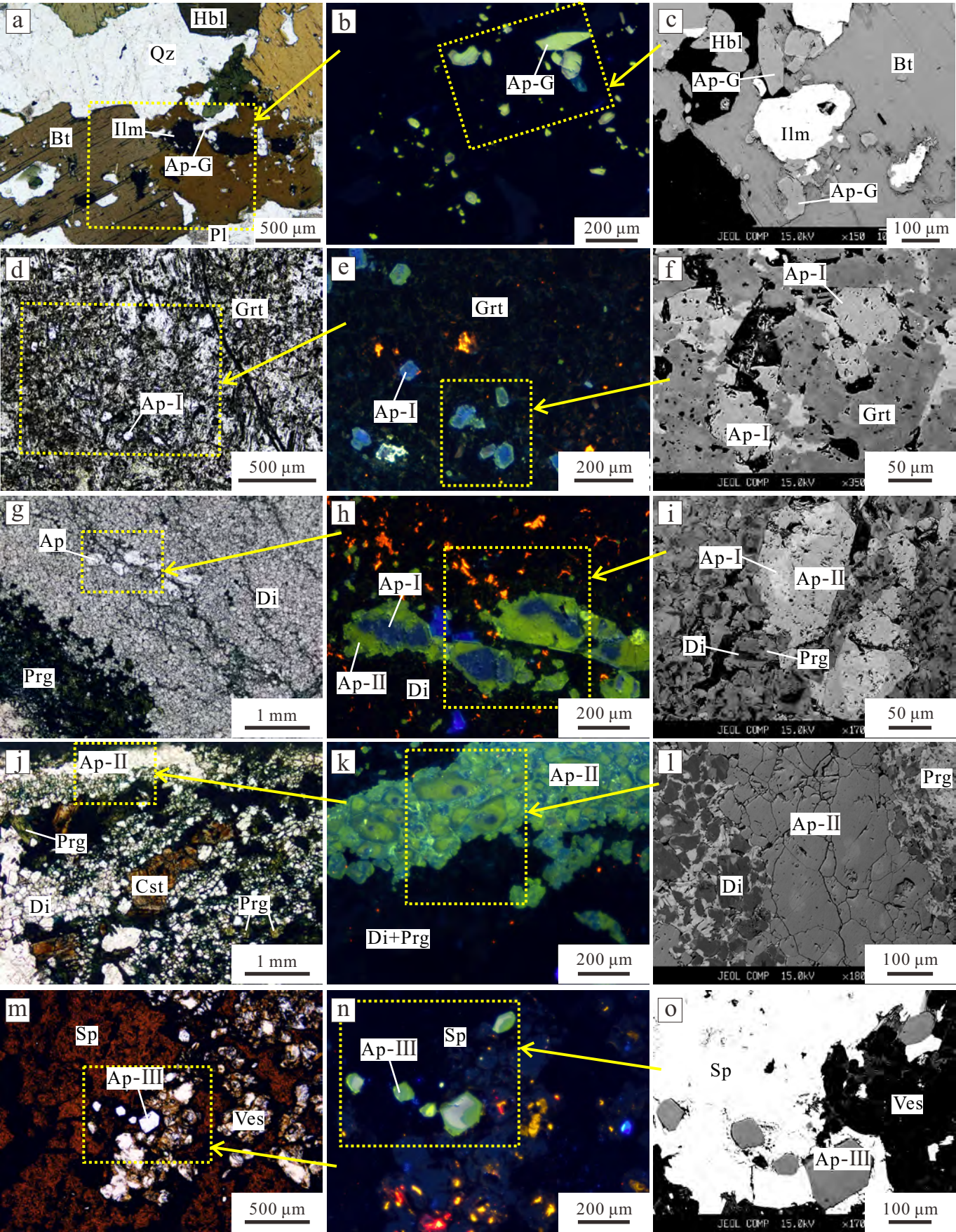
a
Hbl
Qz
Bt
Ilm
Ap-G
Pl
500 μm
b
Ap-G
200 μm
c
Hbl
Ap-G
Bt
Ilm
Ap-G
JEOL COMP 15.0kV ×150
100 μm
d
Grt
Ap-I
500 μm
e
Grt
Ap-I
200 μm
f
Ap-I
Grt
Ap-I
JEOL COMP 15.0kV ×350
50 μm
g
Ap
Di
Prg
1 mm
h
Ap-I
Ap-II
Di
200 μm
i
Ap-I
Ap-II
Di
Prg
JEOL COMP 15.0kV ×170
50 μm
j
Ap-II
Prg
Cst
Di
Prg
1 mm
k
Ap-II
Di+Prg
200 μm
l
Prg
Ap-II
Di
JEOL COMP 15.0kV ×180
100 μm
m
Sp
Ap-III
Ves
500 μm
n
Ap-III
Sp
200 μm
o
Sp
Ves
Ap-III
JEOL COMP 15.0kV ×170
100 μm

Figure 6

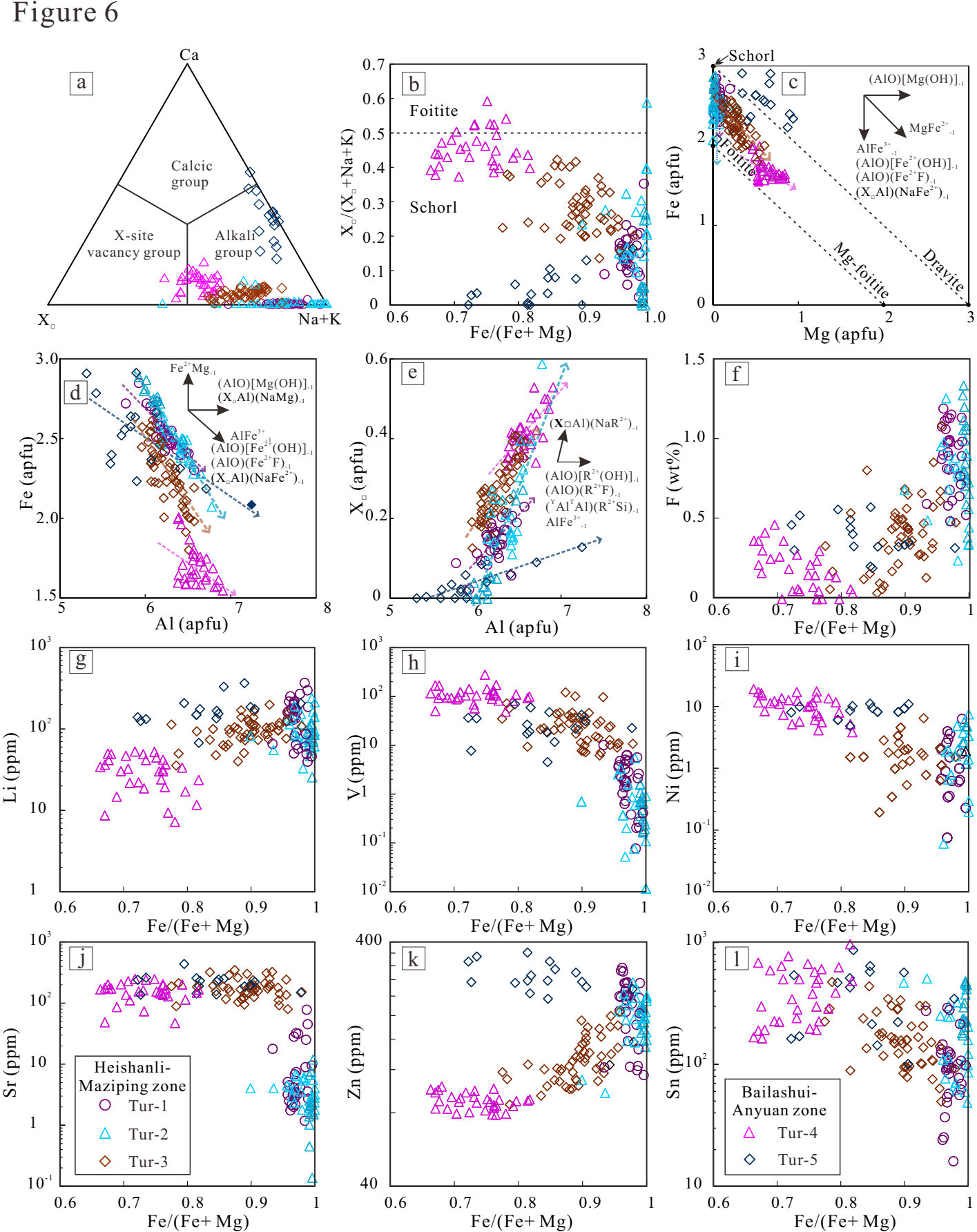
a
Ca
Calcic group
X-site vacancy group
Alkali group
X□
Na+K
b
Foitite
Schorl
X□/(X□+Na+K)
Fe/(Fe+ Mg)
c
Schorl
Foitite
Mg-foitite
Dravite
(AlO)[Mg(OH)]-1
MgFe2+-1
AlFe3+-1
(AlO)[Fe2+(OH)]-1
(AlO)(Fe2+F)-1
(X□Al)(NaFe2+)-1
Fe (apfu)
Mg (apfu)
d
Fe2+Mg-1
(AlO)[Mg(OH)]-1
(X□Al)(NaMg)-1
AlFe3+-1/2
(AlO)[Fe2+(OH)]-1/2
(AlO)(Fe2+F)-1
(X□Al)(NaFe2+)-1
Fe (apfu)
Al (apfu)
e
(X□Al)(NaR2+)-1
(AlO)[R2+(OH)]-1
(AlO)(R2+F)-1
(YAlTAl)(R2+Si)-1
AlFe3+-1
X□ (apfu)
Al (apfu)
f
F (wt%)
Fe/(Fe+ Mg)
g
Li (ppm)
Fe/(Fe+ Mg)
h
V (ppm)
Fe/(Fe+ Mg)
i
Ni (ppm)
Fe/(Fe+ Mg)
j
Heishanli-Maziping zone
Tur-1
Tur-2
Tur-3
Sr (ppm)
Fe/(Fe+ Mg)
k
Zn (ppm)
Fe/(Fe+ Mg)
l
Bailashui-Anyuan zone
Tur-4
Tur-5
Sn (ppm)
Fe/(Fe+ Mg)

Figure 7

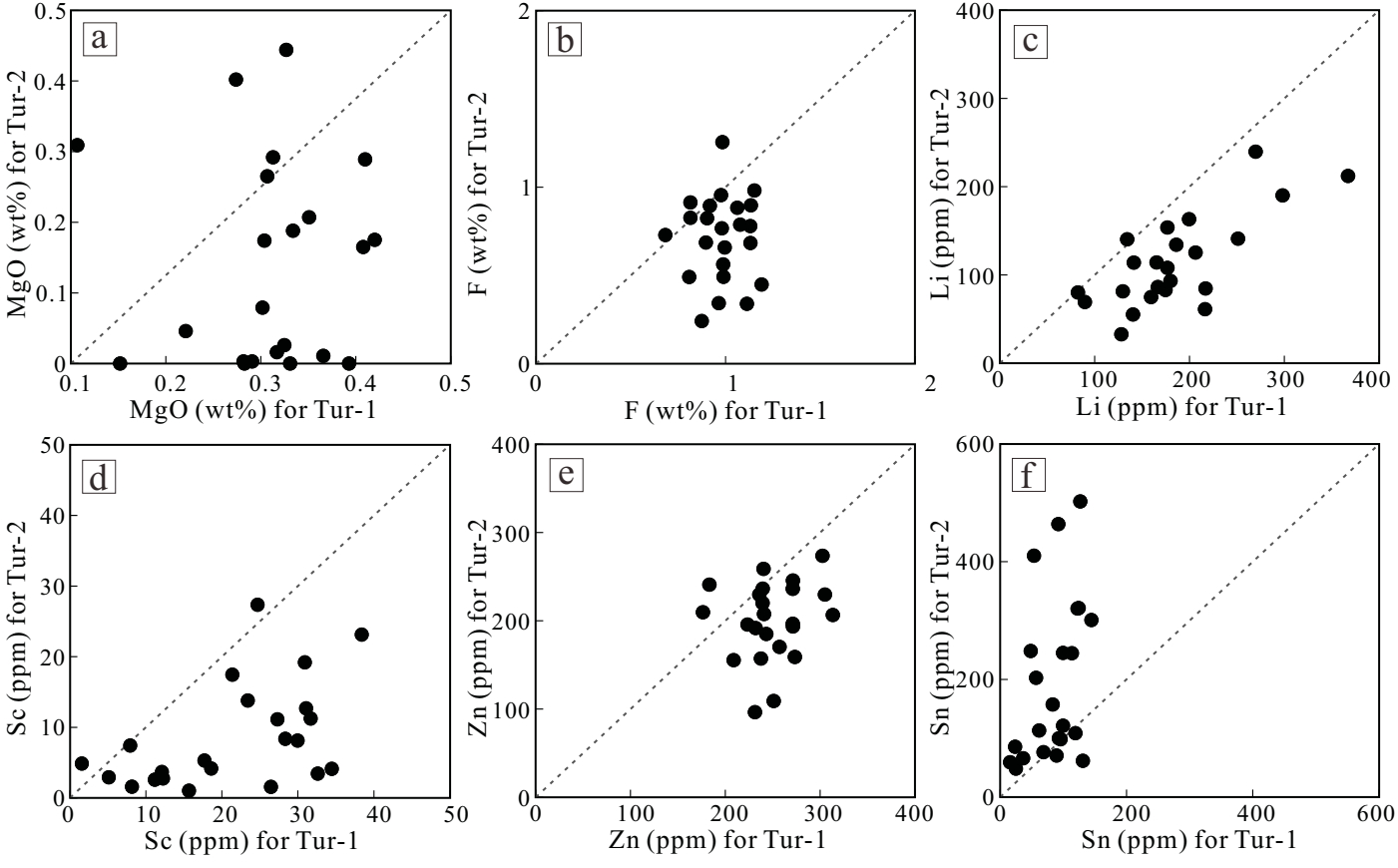
a
MgO (wt%) for Tur-2
MgO (wt%) for Tur-1
0.5
0.4
0.3
0.2
0.1
0
0.1
0.2
0.3
0.4
0.5
b
F (wt%) for Tur-2
F (wt%) for Tur-1
2
1
0
0
1
2
c
Li (ppm) for Tur-2
Li (ppm) for Tur-1
400
300
200
100
0
0
100
200
300
400
d
Sc (ppm) for Tur-2
Sc (ppm) for Tur-1
50
40
30
20
10
0
0
10
20
30
40
50
e
Zn (ppm) for Tur-2
Zn (ppm) for Tur-1
400
300
200
100
0
0
100
200
300
400
f
Sn (ppm) for Tur-2
Sn (ppm) for Tur-1
600
400
200
0
0
200
400
600

Figure 8

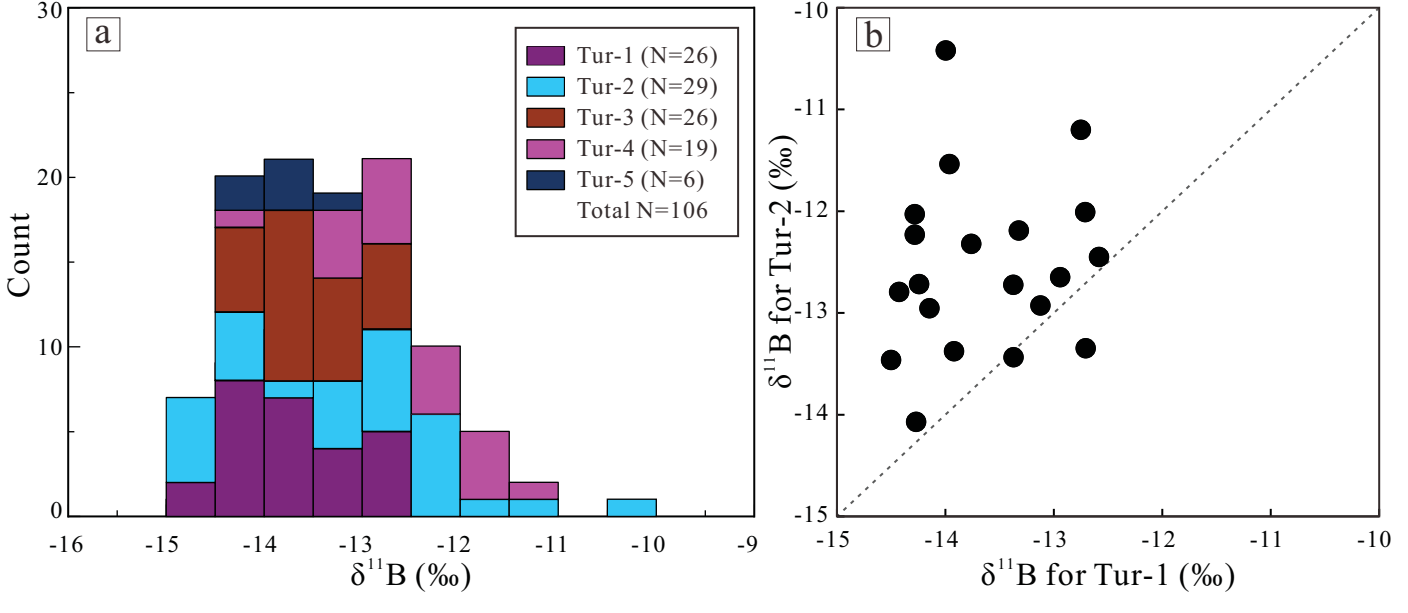
a
Tur-1 (N=26)
Tur-2 (N=29)
Tur-3 (N=26)
Tur-4 (N=19)
Tur-5 (N=6)
Total N=106
Count
δ11B (‰)
b
δ11B for Tur-2 (‰)
δ11B for Tur-1 (‰)

Figure 9

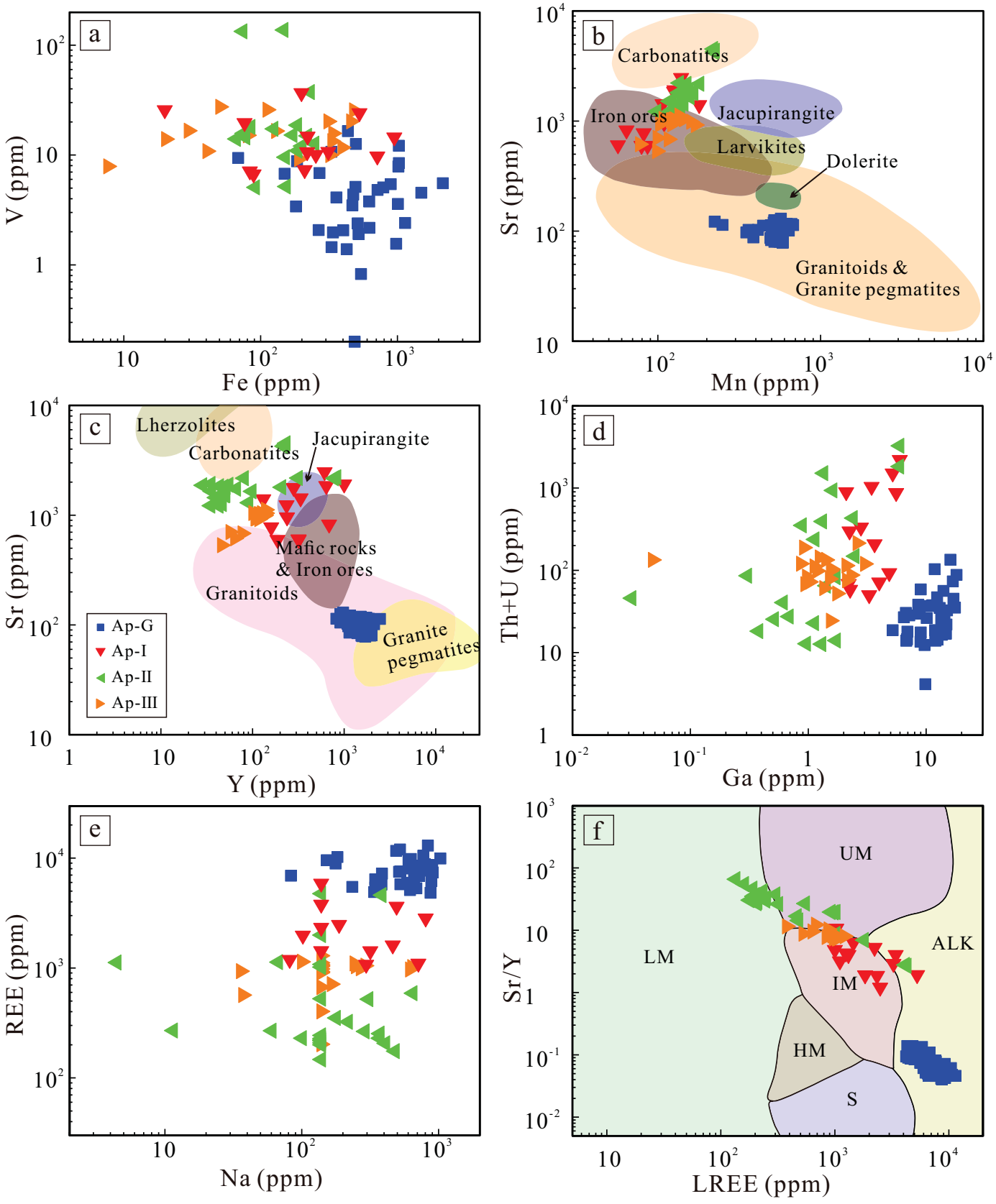
a
V (ppm)
Fe (ppm)
b
Carbonatites
Iron ores
Jacupirangite
Larvikites
Dolerite
Granitoids &
Granite pegmatites
Sr (ppm)
Mn (ppm)
c
Lherzolites
Carbonatites
Jacupirangite
Mafic rocks
& Iron ores
Granitoids
Granite
pegmatites
Ap-G
Ap-I
Ap-II
Ap-III
Sr (ppm)
Y (ppm)
d
Th+U (ppm)
Ga (ppm)
e
REE (ppm)
Na (ppm)
f
UM
LM
ALK
IM
HM
S
Sr/Y
LREE (ppm)

Figure 10

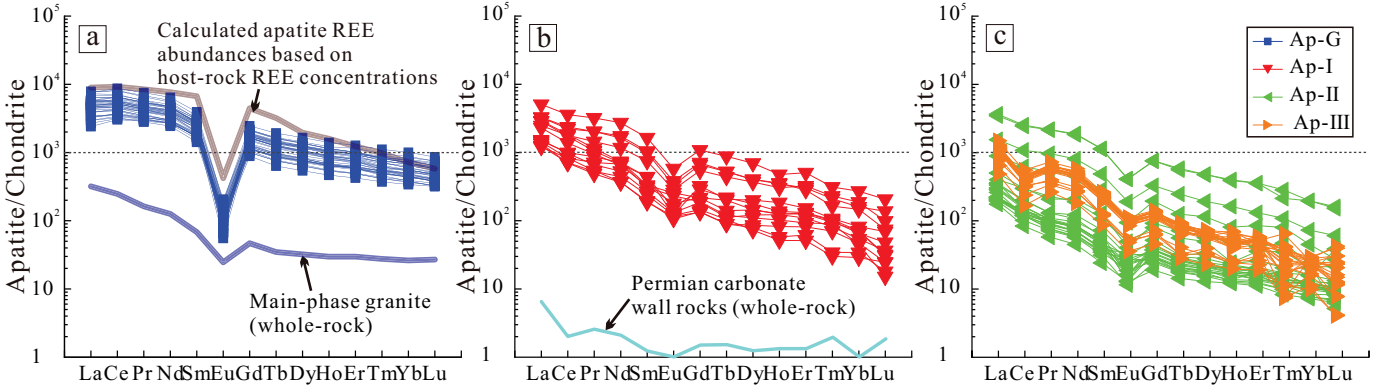
a
Calculated apatite REE abundances based on host-rock REE concentrations
Main-phase granite (whole-rock)
Apatite/Chondrite
b
Permian carbonate wall rocks (whole-rock)
c
Ap-G
Ap-I
Ap-II
Ap-III
La Ce Pr Nd Sm Eu Gd Tb Dy Ho Er Tm Yb Lu

Figure 11

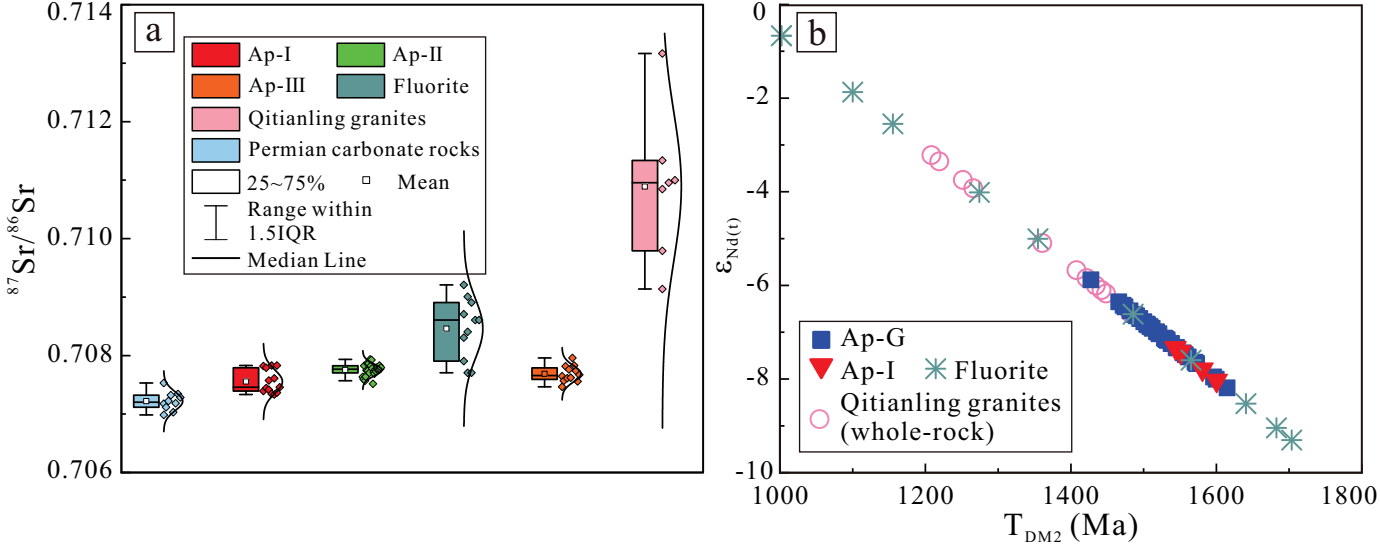
a
Ap-I
Ap-II
Ap-III
Fluorite
Qitianling granites
Permian carbonate rocks
25~75%
Mean
Range within 1.5IQR
Median Line
$^{87}Sr/^{86}Sr$
0.714
0.712
0.710
0.708
0.706
b
$\varepsilon_{Nd(t)}$
0
-2
-4
-6
-8
-10
Ap-G
Ap-I
Fluorite
Qitianling granites (whole-rock)
1000
1200
1400
1600
1800
T_{DM2} (Ma)

Figure 12

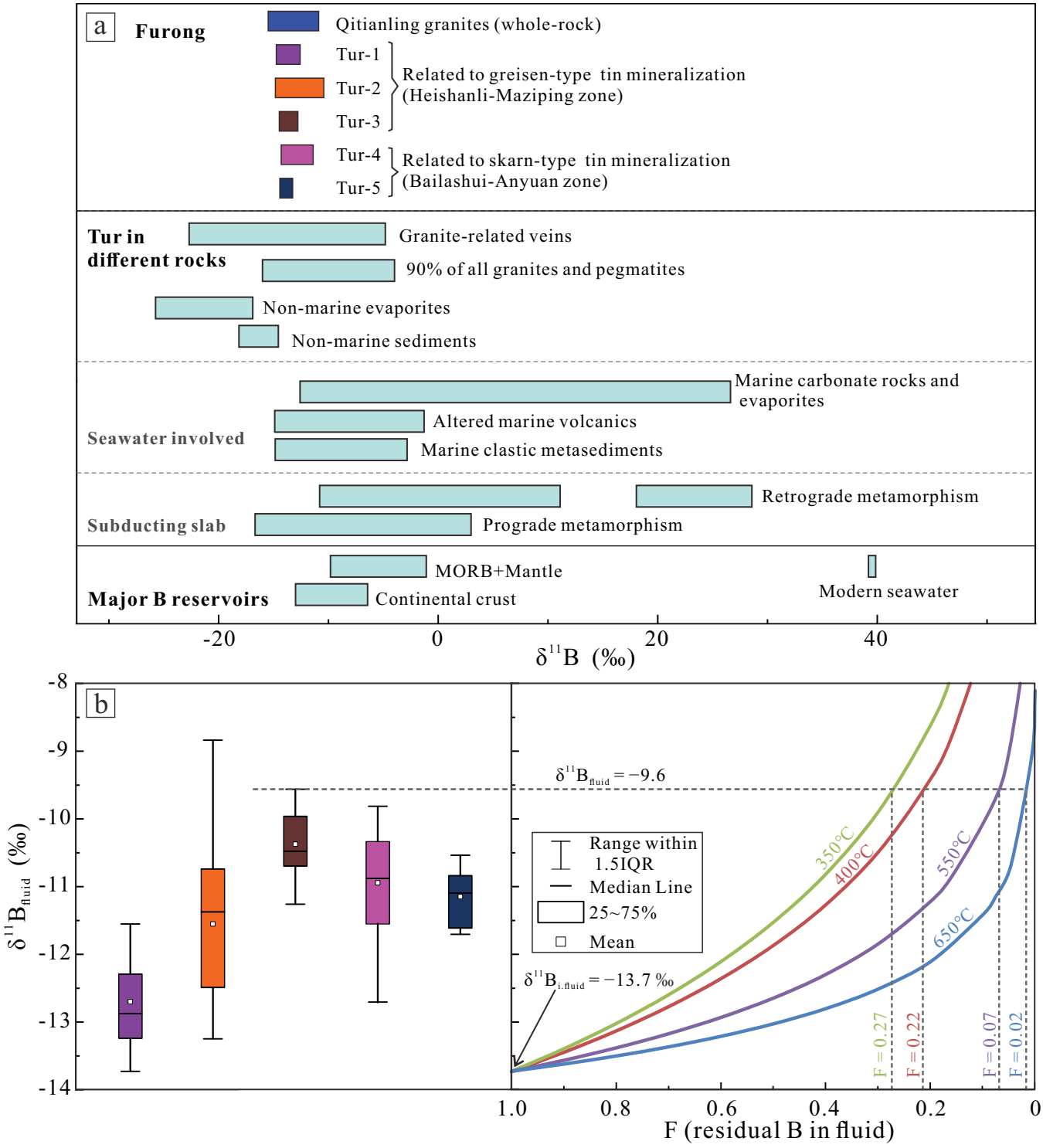
a
Furong
Qitianling granites (whole-rock)
Tur-1
Tur-2
Tur-3
Related to greisen-type tin mineralization
(Heishanli-Maziping zone)
Tur-4
Tur-5
Related to skarn-type tin mineralization
(Bailashui-Anyuan zone)
Tur in different rocks
Granite-related veins
90% of all granites and pegmatites
Non-marine evaporites
Non-marine sediments
Seawater involved
Marine carbonate rocks and evaporites
Altered marine volcanics
Marine clastic metasediments
Subducting slab
Retrograde metamorphism
Prograde metamorphism
Major B reservoirs
MORB+Mantle
Continental crust
Modern seawater
-20
0
20
40
δ11B (‰)
b
δ11Bfluid (‰)
-8
-9
-10
-11
-12
-13
-14
δ11Bfluid = −9.6
Range within 1.5IQR
Median Line
25~75%
Mean
δ11Bi.fluid = −13.7 ‰
350°C
400°C
550°C
650°C
F = 0.27
F = 0.22
F = 0.07
F = 0.02
1.0
0.8
0.6
0.4
0.2
0
F (residual B in fluid)